

**Department of Physics and Astronomy
University of Heidelberg**

Master Thesis in Physics
submitted by

Maurus Hans

born in Hadamar (Germany)

2017

**An experimental setup
for a potassium Bose-Einstein condensate
with tunable interactions**

This Master thesis has been carried out by Maurus Hans at the
Kirchhoff-Institute for Physics in Heidelberg
under the supervision of
Prof. Dr. Markus K. Oberthaler

An experimental setup for a potassium Bose-Einstein condensate with tunable interactions

This thesis gives an overview of the experimental system of a newly designed experiment, that aims for research with Bose-Einstein condensed potassium. The vacuum system and the laser setup are summarised. Afterwards the design and setup of magnetic field coils are discussed. The supply systems are illustrated with focus on the current control with a passbank. With their actual geometry the magnetic coils are simulated to estimate their performance. For the homogeneous field a strength of 3.97 G/A was found with a relative deviation of less than 1.5×10^{-6} in a region of $\pm 100\ \mu\text{m}$. The gradient field reaches 0.91 G/(cmA) on the strong axis. Finally a magneto-optical trap was achieved and the number of trapped atoms was estimated to be 2.6×10^8 using the fluorescence of the atom cloud.

Ein experimenteller Aufbau für ein Bose-Einstein-Kondensat mit einstellbarer Wechselwirkung

Diese Arbeit gibt einen Überblick über das experimentelle System eines neu entwickelten Experimentes, das auf die Forschung mit Bose-Einstein kondensiertem Kalium abzielt. Das Vakuumsystem und der Laseraufbau werden zusammengefasst. Danach wird die Entwicklung und der Aufbau von Magnetfeldspulen diskutiert. Deren Versorgungssysteme werden mit Fokus auf die Stromkontrolle mit einer Passbank beschrieben. Die Magnetfeldspulen werden mit ihrer tatsächlichen Geometrie simuliert, um ihre Leistungsfähigkeit zu ermitteln. Für das homogene Feld wurde eine Stärke von 3.97 G/A mit einer relativen Abweichung von weniger als 1.5×10^{-6} in einer Region von $\pm 100\ \mu\text{m}$ bestimmt. Das Gradientenfeld erreicht 0.91 G/(cmA) auf der starken Achse. Schließlich wurde eine magneto-optische Falle erreicht und die Anzahl der gefangenen Atome durch die Fluoreszenz der Atomwolke zu 2.6×10^8 bestimmt.

Contents

1. Introduction	9
2. Theoretical background	11
2.1. Cooling and trapping	11
2.2. Scattering length and Feshbach resonances	13
2.3. Properties of potassium	15
3. Experimental setup	19
3.1. Vacuum system	19
3.2. Laser system	21
3.3. Atom source	21
4. Magnetic Coils	23
4.1. Design	23
4.2. Setup in the experiment	28
4.3. Performance	29
4.4. Passbank	33
5. Characterisation of the ^{39}K MOT	37
6. Conclusion and Outlook	41
A. Technical drawings	43
A.1. Multicoils	43
A.2. Passbank	44
A.3. Current connector	46
A.4. Water splitter	46
A.5. Holder for vacuum chamber	47
A.6. Housing for optical table	48
B. Numerical integration scheme	49

1. Introduction

Since the first successful experimental approaches to laser cooling of atomic vapours [1, 2] in the 1980s a whole new research field has developed. The route to lower temperatures finally led to the experimental realisation of Bose-Einstein condensation [3, 4] in 1995. A Bose-Einstein condensate (BEC) is an extremely pure macroscopic and isolated state. It can thus be used as a good model system for the dynamics of many-body systems. When Feshbach resonances were first observed in 1998 [5] this increased the possibilities for study and manipulation of BECs enormously [6]. It became possible to change the atomic interaction and gain access to various regimes of many-body dynamics.

One particularly promising atom species is the bosonic ^{39}K . It has a small background scattering length and a broad Feshbach resonance [7]. On one side, this allows for precise tuning of the atomic interaction to a noninteracting condensate. In this scope research about atom interferometry [8], Anderson localisation [9] and magnetic dipolar interactions [10] has been done. On the other side, going closer to the Feshbach resonance strongly interacting or even unitary systems can be prepared as well. Nonetheless, in this regime significant particle loss and heating occur. Compared to other species the three-body loss coefficient is reduced for ^{39}K due to species-specific Efimov physics [11]. This makes it a promising candidate for research in many-body systems at unitarity. Recently, quantum droplets have been observed in a spinor condensate of ^{39}K [12]. They form due to small attractive inter-species and repulsive intra-species interactions, which can be prepared exploiting Feshbach resonances.

However, condensation of ^{39}K is cumbersome and was achieved only in 2007 using sympathetic cooling [13]. Reaching the BEC phase without an additional coolant has been demonstrated in [14] due to a new sub-Doppler cooling scheme in 2012. Even an all-optical [15] scheme was developed two years later.

This thesis describes an experimental setup for the work with ^{39}K . After introducing the basic concepts an overview of the experimental setup is given. The thesis then focusses on the setup of the magnetic fields in the experimental region. The design, setup and supply systems of magnetic coils are described and their performance is evaluated with a simulation. Finally the particle number of a ^{39}K cloud trapped in a magneto-optical trap is estimated. In an outlook further steps towards a BEC of ^{39}K are illustrated.

2. Theoretical background

This chapter gives a short overview of the concepts of neutral atom trapping. The concept of Feshbach resonances is presented, which allow to tune the interaction of atoms with background magnetic fields. Afterwards the relevant properties of potassium are summarised and it is discussed that a modification of the interaction is necessary to reach quantum degeneracy of potassium.

2.1. Cooling and trapping

To gain an intuitive understanding of the cooling and trapping of atoms one can study a two-level system and its interplay with light. This section is based on [16, 17] and a derivation can be found there.

Two-level system In the most cases it is possible to gain an understanding of the interaction of atoms and light by the reduction of the atomic system to a two level system. One of the simplest models describing an atom is the two-level system. It assumes that the atom has a ground state $|g\rangle$ and an excited state $|e\rangle$. They are both eigenstates of a time-independent Hamiltonian. Their energy difference sets the atomic resonance frequency, $\Delta E = \hbar\omega_{eg}$. If this system is coupled to an external monochromatic light field with frequency ω_L close to the resonance frequency the Hamiltonian is changed and the above mentioned states are no longer eigenstates. Instead, the state of the atom is a time-dependent superposition of ground and excited state.

To calculate the state of the atom one commonly solves the time-dependent Schrödinger equation assuming the rotating wave and dipole approximation. The first assumes that the detuning $\delta = \omega_{eg} - \omega_L$ is small. The latter holds when the light field has a wavelength greater than the size of the atom, which means that the spatial variation of the light field over the atom is neglected. This ansatz leads to an oscillation between ground and excited state depending on the detuning δ and the so-called Rabi frequency Ω which is the oscillation frequency between ground and excited state in the limit of no detuning.

This model neglects an important property of the excited state, namely its finite life time. Up to now only stimulated processes were included, but real atoms can decay from the excited to the ground state spontaneously as well. This leads to an exponential decay of the excited. It has a life time of $1/\gamma$. Incorporating this into the developed formalism leads to the *Optical Bloch equations* that describe the dynamics of a coupled two-level system.

Due to the Rabi oscillation one can observe a saturation as the intensity of the light field rises. If the system is in a steady state the probability to be in the excited state ρ_{ee} can not exceed $1/2$. This saturation process can be described by the *saturation parameter*,

$$s = \frac{2\Omega^2}{\gamma^2} = \frac{I}{I_s}, \quad (2.1)$$

where I_s is the intensity at which the transition starts to saturate. Consequently the scattering rate γ_{sc} depends on the probability to be in the excited state ρ_{ee} and therefore on the saturation parameter,

$$\gamma_{sc} = \gamma\rho_{ee} = \frac{\gamma}{2} \frac{s}{1 + s + (2\delta/\gamma)^2}. \quad (2.2)$$

As one would expect, this saturates to $\gamma/2$ for large intensities.

Magneto-optical trap When atoms absorb and emit light momentum is transferred between photons and atoms. If photons from a certain direction are absorbed and the atom decays spontaneously in free space the photons are emitted in random directions. This leads to a transfer of a net momentum.

Extending the simple picture of the two-level system the atom is allowed to move in one spatial dimension with a velocity v . For a magneto-optical trap two counter-propagating monochromatic light beams of frequency ω_L are shone in on the atom. Their frequencies are shifted in the reference frame of the atom due to the Doppler shift. The beam propagating parallel to the atom's velocity is red-detuned (lower effective frequency) and the other beam is blue-detuned (higher effective frequency) by kv , where k is the wave vector of the photon. Hence, the frequency of one beam will be further away from the atomic resonance frequency, the atom scatters less photons and less momentum is transferred. This can be used to slow down the atom. If one chooses the light frequency of the two beams lower than the atomic resonance it has to be shifted to a higher frequency to interact with the atom. This can only happen if the atom moves towards a light beam and it appears blue-detuned. The atom then scatters photons and gets slower. In three dimensions with two counter-propagating beams along each dimension this scheme can be used to cool atoms and confine them in momentum space. The cooling scheme is called *optical molasses*.

To confine the atom in position space a linear magnetic field gradient with a zero crossing can be used. For simplicity the problem is restricted to one dimension again. The magnetic field leads to a Zeeman splitting of atomic levels into sub-levels. For the model the ground state is assumed to be $J = 0$ and the excited $J = 1$. The excited state splits into three substates $M_J = -1, 0, +1$ depending on the strength of the magnetic field B . If the quantisation axis is chosen in the direction of the magnetic field the sub-levels shift like $\Delta E \sim M_J|B|$ as shown in Figure 2.1. The state $J = 0$ has only one sub-level $M_J = 0$ which is not affected by the magnetic field.

Transitions between sub-levels of different M_J are possible with σ light according to the selection rules. Right-handed circularly polarised light is σ^- light if propagates

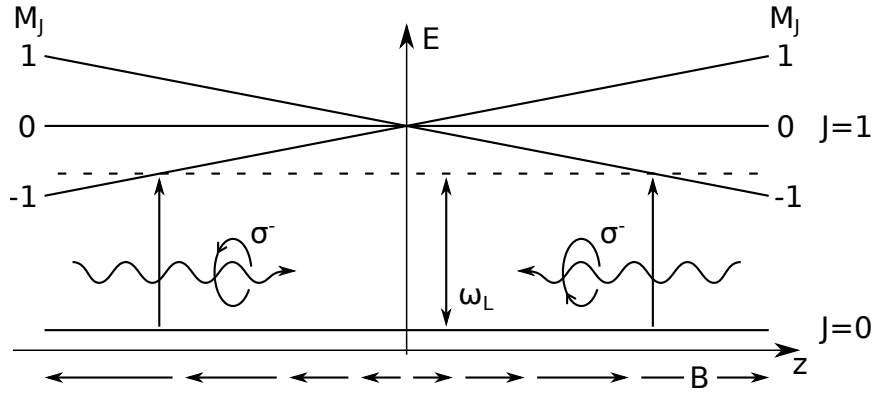


Figure 2.1.: Principle of the magneto-optical trap. A linearly increasing magnetic field B splits the upper state into sublevels. As the incoming light is right-handed circularly polarised and red-detuned it can scatter with the atoms in the $M_J = -1$ substate and support a restoring force. Getting closer to the centre the atoms are shifted out of resonance due to the magnetic field gradient.

anti-parallel to the quantisation axis. With this light transitions from $J = 0$ to $J = 1, M_J = -1$ are allowed. If the same light propagates parallel to the quantisation axis it is σ^+ light and can drive transitions to the $M_J = 1$ sub-state.

This selection rules and the spatially varying magnetic field can be used to confine atoms close to the zero crossing of the magnetic field. As above, two counter-propagating red-detuned laser beams are shone in on the atom. Additionally, they are right-handed circularly polarised. If an atom leaves the zero crossing its magnetic sub-levels of the excited state are shifted. Eventually, the $M_J = -1$ sub-state comes into resonance with the light beam. Due to the selection rules and the polarisation of the counter-propagating beams it can only interact with the one beam that pushes it back to the middle (cf. Figure 2.1). The other beam could excite the atom to the $M_J = 1$ sub-state, but this state is shifted out of resonance. This process provides a restoring force and traps the atom close to the zero crossing of the magnetic field. As before this can be extended to three dimensions and this confinement of atoms in momentum and position space is called *magneto-optical trap* (MOT).

2.2. Scattering length and Feshbach resonances

In ultra-cold atomic vapours near quantum degeneracy very low temperatures and low densities simplify the description of the scattering processes. It becomes possible to describe these events with a single quantity. This so-called scattering length and the possibility to change it using Feshbach resonances will be explained in this chapter based on [18]. A much more detailed discussion can be found there.

The simple treatment of scattering events in ultra-cold gases is applicable when the kinetic energy is very low, leading to a small wave number k and a large wavelength, respectively. Also, the potential of the scatterer has to be short-ranged which is

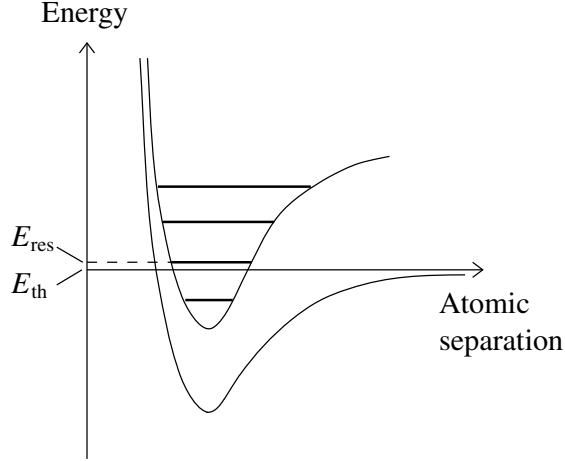


Figure 2.2.: Energy potentials near a Feshbach resonance. As a bound state with energy E_{res} gets close to the threshold energy E_{th} a mixing occurs, which alters the scattering length. Figure from [18].

the case for the often dominant van der Waals interactions. Then, the scale of the particle wavelength is much larger than the scale of the interaction potential and the precise form of the potential plays a minor role. In a formal way this is done with the partial wave expansion, where the outgoing wave is expanded in terms of its angular momentum components. In the considered limit both the wave function of the outgoing particle and the potential of the atom can be approximated by spherically symmetric functions. If the temperature is sufficiently low, higher angular momenta can be neglected and one hence calls the process *s-wave scattering*. The *scattering length* describes this process in terms of the only free parameter, the phase difference of the incoming and outgoing wave,

$$\delta = -ka. \quad (2.3)$$

A negative scattering length represents attractive interaction and vice versa. If the scattering length approaches zero the particles can be regarded as non-interacting. The scattering length is related directly to the scattering cross section. For identical bosons one gets

$$\sigma = 8\pi a^2. \quad (2.4)$$

This approach does not account for higher order processes. One type of processes quite important in the context of potassium are *Feshbach resonances*. They occur, when the energy of a bound state is close to the threshold energy of the particles (cf. Figure 2.2). Depending on the magnetic moment of the atoms the exact energy of the bound state can be shifted with an external magnetic field. As the energy difference between bound state and threshold energy diminishes two atoms can be scattered to an intermediate bound state, which alters the scattering length. With the help of perturbation theory the effect can be calculated in the vicinity of the Feshbach

resonance,

$$a = a_{\text{bg}} \left(1 - \frac{\Delta}{B - B_0} \right), \quad (2.5)$$

where B_0 corresponds to the magnetic field that matches the bound state's energy with the threshold energy, Δ the width of the resonance, defined as difference between B_0 and the magnetic field at the zero crossing of the scattering length, and a_{bg} the background scattering length far away from the resonance.

2.3. Properties of potassium

In the following the properties and peculiarities of ^{39}K will be discussed and an experimental roadmap to tackle the arising problems will be presented.

^{39}K is the most abundant natural potassium isotope and a bosonic species. Its strongest optical transitions are shown in Figure 2.3. The hyperfine splittings are drawn to scale and one can see that $^2P_{3/2}$ has an extremely narrow splitting. Keeping in mind that the natural line width for this transition is $2\pi \times 6.035$ MHz [19] it is hard to separate the different lines, which has consequences for laser cooling of potassium.

To trap ^{39}K in a MOT it is preferable to use a transition which atoms can not escape. The most natural choice is the transition $^2S_{1/2} F = 2$ to $^2P_{3/2} F = 3$. Due to the selection rules an atom can only decay back to the $^2S_{1/2} F = 2$ state and is excited again. Since the linewidth of this transition is in the order of the splitting of the sub-levels in the excited state the $^2P_{3/2} F = 2$ state becomes populated as well. From this state atoms can decay to the $^2S_{1/2} F = 1$ state. Once in this state, the atoms can not be excited and cooled anymore. To circumvent this a second light frequency is needed that excites the atoms from the $^2S_{1/2} F = 1$ to the $^2P_{3/2} F = 2$ state. For both frequencies roughly the same light intensity is needed and they both take equal parts in the cooling and trapping of the atoms.

After the atoms are captured in the MOT it is advantageous to proceed with sub-Doppler cooling on the path to quantum degeneracy. A commonly used technique is the Sisiphus cooling mechanism [20, 21] as it can often be done with the MOT light. However, as the hyperfine manifold of the D2 transition is so narrow a beam red-detuned to the $^2P_{3/2} F = 3$ excited substate is also blue-detuned to the $F = 2$ substate. This results in heating and therefore makes efficient cooling difficult. To overcome this a cooling scheme called grey molasses has been demonstrated. It uses D1 light which is blue-detuned to the $^2P_{1/2} F = 2$ substate and temperatures as low as 6 μK have been reached [22].

To reduce the temperature of the sample further, evaporative cooling [24] is often used. From a technical perspective, one has to choose between two paths at this point. Either the atom sample can be loaded directly into a dipole trap [15]. This requires high laser powers in order to obtain a deep and wide trap as the atomic cloud is still rather hot. If this is not possible an intermediate stage of magnetic trapping is needed. In both cases the cooling takes place by reducing the trap depth. This allows atoms with high energy to leave the trap. Meanwhile the remaining atoms rethermalise

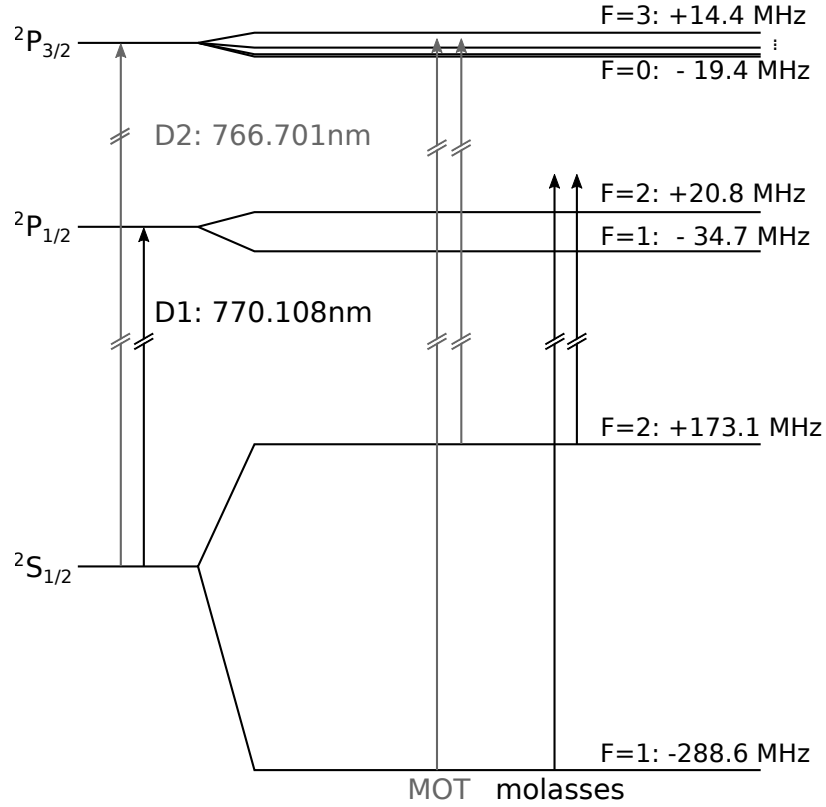


Figure 2.3.: Level scheme of ^{39}K . The hyperfine splittings are drawn to scale. One can see that the splitting of $^2P_{3/2}$ is extremely narrow compared to the transition's linewidth of $2\pi \times 6.035$ MHz which makes efficient cooling difficult. The transitions for MOT and grey molasses are sketched as well. Values taken from [19].

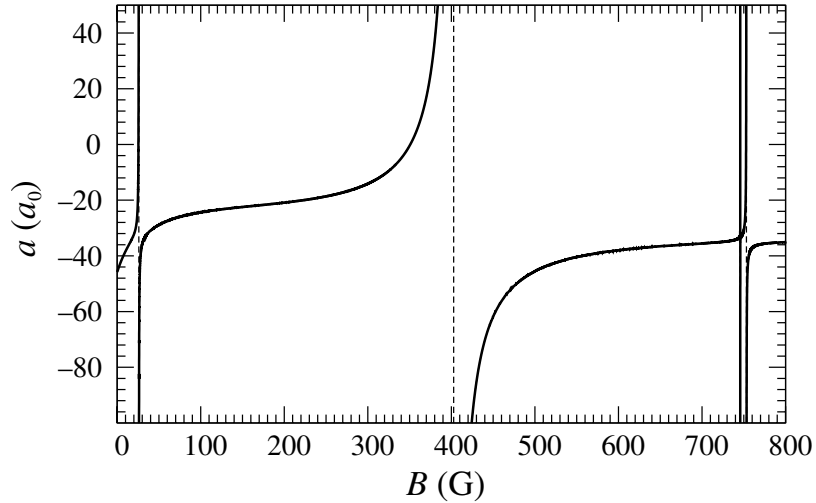


Figure 2.4.: Feshbach resonance of the $^2P_{1/2}$ $F=1$ hyperfine state of ^{39}K . The Feshbach resonance is located at 403 G, has a width of $\Delta = -52$ G and background scattering length of $a_{\text{bg}} = -29 a_0$ (with a_0 the Bohr radius). Figure and values from [23].

and the mean energy is reduced. At this point another obstacle arises. For decent rethermalisation the atoms have to interact and exchange momentum, which can be described with the help of the scattering length as discussed above. Looking at Figure 2.4, one can see that the background scattering length $a_{\text{bg}} = -29 a_0$ is rather small leading to slow rethermalisation (with a_0 the Bohr radius). Furthermore, the scattering length is negative, which means the interaction is attractive. On one side, this gives rise to the so-called *Ramsauer-Townsend minimum* [25]. This is a dependence of the intraspecies scattering length on the temperature in a specific window. ^{39}K exhibits this minimum around $320 \mu\text{K}$. It can cause problems for evaporative cooling, which heavily relies on the interaction of the atoms. It is therefore best to cross this minimum with laser cooling processes such as grey molasses. On the other side, the attractive interaction can lead to a collapse and complete loss of the atom cloud when reaching quantum degeneracy [26, 27].

In the dipole trap the scattering length can be tuned with an external magnetic field using the broad Feshbach resonance described above. Therefore it is desirable to load the atom cloud to the dipole trap as soon as possible. The tuning of the scattering length allows not only to prevent the collapse but also to enhance the rethermalisation process by setting it to about $180a_0$ [13]. With the help of the Feshbach resonance quantum degeneracy can be reached.

3. Experimental setup

For trapping and experimenting with atoms at quantum degeneracy ultra-high vacuum conditions and a stable environment for the experiment are needed. The setup to achieve this will be described in the following. Afterwards a short overview of the laser system will be given. In the scope of the experiment a 2D-MOT [28] is used to pre-cool atoms and guide them to the experimental region, which will be explained in the last section.

3.1. Vacuum system

The vacuum system used for the experiment has been designed and built up for mixture experiments with potassium and rubidium [25, 29]. It was later used to study rubidium atoms in a dissipative double well potential with single atom resolution [30, 31]. A sketch of the system is shown in Figure 3.1.

The system consists of two subsystems connected by a differential pumping stage, which is implemented by a thin tube (150 mm length and 5 mm diameter). For both chambers ion sputter pumps are used to maintain the vacuum in the setup and the differential pumping stage allows for different pressures in the two subsystems. While in the experimental chamber a pressure in the order of 10^{-11} mbar is achieved the pressure in the 2D-MOT chamber can be significantly higher due to the very low conductance of the thin tube. By heating the potassium oven a pressure of roughly 10^{-8} mbar is set. This allows to capture atoms from the background (cf. section 3.3).

At the end of the experimental chamber a glass cell is mounted. It is $3.8 \text{ cm} \times 3.8 \text{ cm}$ wide and about 8 cm long. The walls are fabricated of glass with a thickness of 3.8 mm. Using a glass cell has the advantage of high optical access. Also, magnetic coils can be placed close to the experimental region to achieve high field strengths.

The vacuum system was transferred to a new optical table to provide enough space. To ensure laser safety and stability of the setup the table is equipped with a housing. It is free-standing to be decoupled from the table and built from Item aluminium profiles (cf. section A.6). Opaque laser curtains are installed around the table and the top of the housing was closed with wooden multiplex boards. Their stability allows to place supplies for the experiment on top and holes for feedthroughs can easily be added. Furthermore a ventilation system was set up consisting of four flow boxes that are fixed to the Item frame (cf. Figure 3.2). They provide a laminar flow of filtered air. This reduces dust deposition and is especially important for high power lasers as they can acquire dust in the beam which leads to flickering and dusty mirrors. Additionally a heater was included in order to stabilise the air temperature.

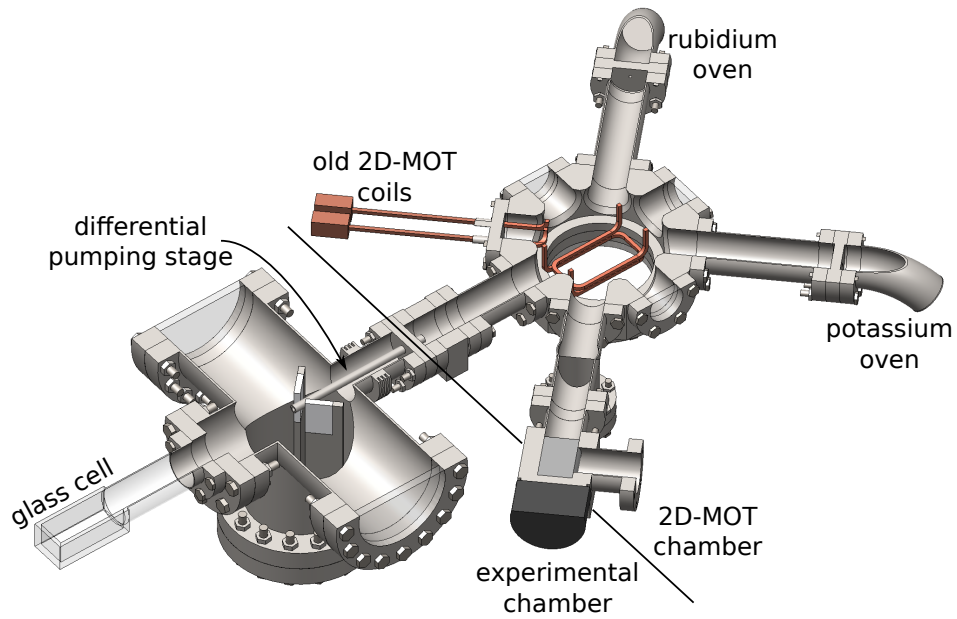


Figure 3.1.: Vacuum system of the experiment. The system includes a 2D-MOT chamber with high pressure. Using a 2D-MOT an atom beam can enter the experimental chamber through a differential pumping stage. In the glass cell the atoms are captured in a MOT and further experimental steps take place. The system was initially set up as a mixture experiment of rubidium and potassium. Image taken from [29].

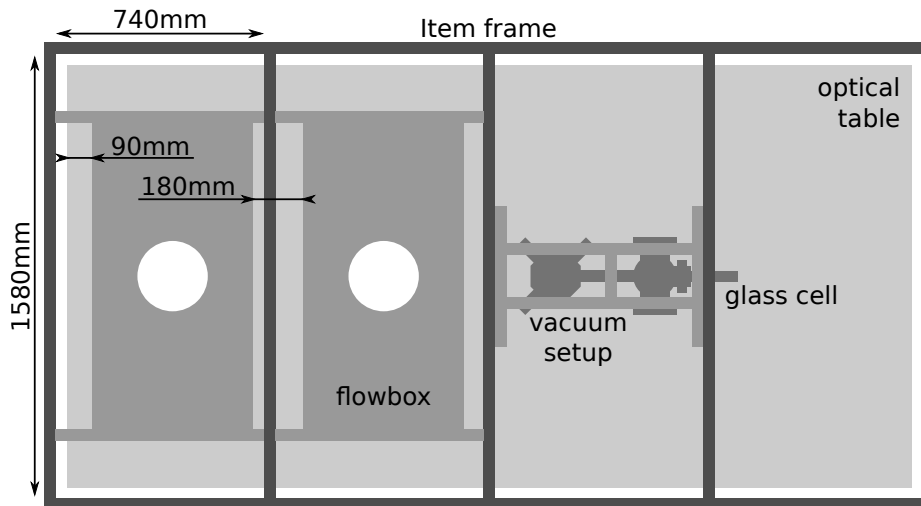


Figure 3.2.: Top view of the optical table with vacuum system and housing. The flowboxes are symmetric to the middle and the rightmost two are not drawn. Instead the position of the vacuum system on the optical table is shown. The Item frame is closed on top with four wooden multiplex boards and on the sides with opaque laser curtains.

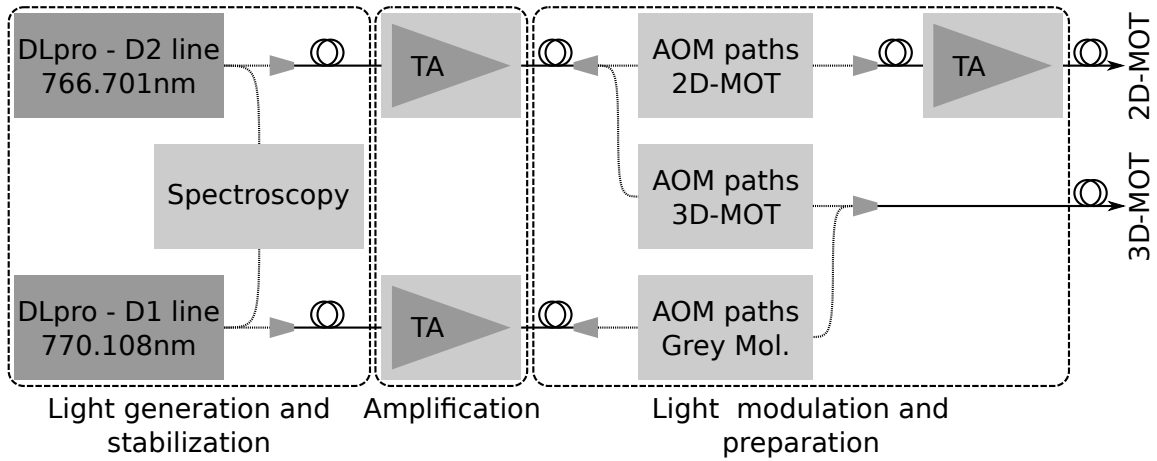


Figure 3.3.: Overview of the lasersystem. The system consists of three parts. In the first part the light is produced by two ECDLs for D1 and D2 light, respectively. Both are locked to a doppler free saturation spectroscopy. Afterwards the light is amplified with a TA for each frequency. In a final stage the different frequencies necessary are produced using AOM paths. They are coupled into fibres that guide the light to the experiment.

3.2. Laser system

A rough sketch of the of the laser system is shown in Figure 3.3. The starting point are two Topitca DLpro external cavity diode lasers (ECDL). With a doppler free spectroscopy they are locked to the D1 line at 770.108 nm [19], respectively, and coupled into fibres. The light is then fed into a tapered amplifier (TA) for each wavelength and gets amplified. The TA unit is fully fibre-coupled and was developed throughout [32]. After the amplification stage the light is split and shifted to the frequencies necessary for the experiment with the help of acusto-optic modulators (AOM). Coupled again into fibres it is guided to the experiment. A more detailed description of the setup and its single components can be found in [33].

3.3. Atom source

For the experiments under ultra-high vacuum conditions an atom source is needed. Direct loading of the MOT in the experimental chamber from the background is not possible at the desired background pressure. Instead, a 2D-MOT [28] is implemented in a second vacuum chamber with a higher background pressure. It is loaded from the background and acts as an atom source for the 3D-MOT. It consists of two perpendicular pairs of counter-propagating laser beams leading to a cigar-shaped MOT that emits transversally cooled atoms at its ends. If the MOT is aligned with the differential pumping stage and adjusted properly the beam of pre-cooled atoms

can pass through and load a 3D-MOT in the experimental chamber. For further enhancement a push beam can be used. It is shone in along the radial symmetry axis of the cigar-shaped atom cloud. The push beam closes the 2D-MOT on one end and provides additional momentum in the direction of the 3D-MOT.

To produce the magnetic field for the 2D-MOT the vacuum setup features a water cooled coil with one winding in racetrack configuration inside the vacuum [25]. However, this coil was deformed when it was built in. It is likely that this led to a reduced flux, which was no issue for former experiments as they were done with few particles over a long time. For the planned upcoming experiments on the other hand a large MOT is required to provide a sufficient number of atoms for the evaporative cooling stage. Also, a fast loading of the 3D-MOT is desired to reach high repetition rates.

Therefore, a set of new coils was built in. It consists of two elongated rectangular coils with 100 windings distributed over four layers each and is wound from $1\text{ mm} \times 4\text{ mm}$ copper wire. The coils measure $30\text{ cm} \times 15\text{ cm}$ and are placed on top and below the 2D-MOT chamber along the symmetry axis of the beam line.

4. Magnetic Coils

After discussing the setup of vacuum and laser system, and the source of the atoms the focus lies on the experimental chamber. A quite important task is the production of magnetic fields in this region. Throughout the experimental sequence different configurations are needed. During the early stages a gradient field in the order of 10 G/cm is desired to create a MOT. If directly loading the MOT to the dipole trap is not possible a preferably high gradient field is necessary in order to create a large and deep magnetic trap as an intermediate step. To finally achieve condensation and later prepare the BEC in different regimes a homogeneous magnetic field is required to tune the s-wave scattering length using a Feshbach resonance.

If only a homogeneous magnetic field was needed, one could for example use an elongated coil. However, this strongly reduces the optical access in the experimental region. To improve this a pair of coils in Helmholtz distance can be used. They provide a high field homogeneity and optical access. Also, they can produce a gradient field if they are operated with opposite currents. Starting from this ideal system the design decisions for the coils are discussed in the following. Afterwards a description of the setup in the experiment and of the supply systems follows. The magnetic coils were scanned and simulated with this data to evaluate their performance. Finally the design of a passbank for current control is discussed.

4.1. Design

For an ideal coil optimal configurations exist both for homogeneous and linear gradient fields. However, the optimal distance a between two coils with radius r for a homogeneous field is $a = r$, where first and second order derivatives vanish in the centre (Helmholtz configuration). Contrarily, for a linear gradient field $a = \sqrt{3}r$ yields vanishing second and third order derivatives in the centre, sometimes referred to as Anti-Helmholtz configuration. To incorporate those different optima one could choose to use two different sets of coils for each application. Instead, to keep things simple and save space it was decided to use one set of coils and switch the current of one coil according to the required field. There is no optimal configuration in this case, but since the coils will consist of more than one wire which also has a spatial extent, a trade-off is necessary in any case. The coils will be referred to as *multicoils* in the following due to their application for different magnetic field configurations.

From a technical perspective the design is restricted by the size of the experimental chamber. Its height is 3.8 cm and therefore sets the minimal distance between the coils. Furthermore the power supply unit (Agilent 6690A) has an output limit of

440 A at 15 V. With an estimated voltage drop of 3 V for wiring and current control components 12 V remain for driving the current through the coils. This sets a limit on the total wire length. Due to the high currents the coils need an ample cross section and have to be cooled actively. This is achieved by using a hollow copper wire where cooling water can flow through. A quadratic copper wire with a width of 5 mm and a hole of 3 mm diameter was chosen. It has a resistance of 1.017 m Ω /m and therefore limits the total length of wire for the coils to 24.9 m assuming a current of 440 A (corresponds to a drop of 0.48 V/m).

Within this bounds the exact dimensions of the coils have to be determined. From an engineering point of view the coils should consist of double layers of wire (double pancake configuration) since this is the best way to wind coils from thick wire. It is usually done by winding the wire around a cylinder. Its diameter sets the inner diameter of the coils. Starting from the middle of the wire, two loops are laid around the cylinder. With each end of the wire a flat coil is wound outwards. This results in a double pancake structure. In the end the cylinder is removed and the wire is fixed in a form or with casting resin.

The coils were modelled in this double pancake configuration as current loops where the distance between the loops of 5.6 mm is set by the size of the quadratic wire and the Kapton insulation of the wire. To calculate the magnetic fields numerical integration can be used. With help of the Biot-Savart law [34] the magnetic field \mathbf{B} at a point \mathbf{r} generated by a current I along a curve C can be calculated,

$$\mathbf{B}(\mathbf{r}) = \frac{\mu_0}{4\pi} \int_C \frac{I d\mathbf{l} \times \mathbf{r}'}{|\mathbf{r}'|^3} \approx \frac{\mu_0}{4\pi} \sum_i \frac{I \Delta\mathbf{l}_i \times \mathbf{r}'_i}{|\mathbf{r}'_i|^3}, \quad (4.1)$$

with $d\mathbf{l}$ the differential line element and $\mathbf{r}' = \mathbf{r} - \mathbf{l}$ the displacement of the line element from the the point of interest. To solve the integral it can be discretised by splitting the curve into finite line elements $\Delta\mathbf{l}_i$. Using this numerical integration scheme (implementation in Appendix B) the magnetic fields were calculated in a region of 100 μm around the centre. To rate the different configurations three quantities were determined. The total magnetic field in the centre and the homogeneity in the central region were calculated for the symmetric, Helmholtz-like case and the achievable gradient for the Anti-Helmholtz configuration. As the linearity does not play a major role in the latter case it has been neglected.

After initial simulations with different numbers of coils and different sizes it was found out that the available wire length is best distributed using four double pancake coils, two above and two below the glass cell (cf. Figure 4.1 (a)). The distance between the coils above and below the cell should be minimal to reach high field strengths. It was therefore set to 5 cm to keep a safety distance of 5 mm between cell and coil on each side and to increase the optical access. Looking closer at the deviation of the fields around the central point showed that it is sufficient to compare the fields at one point on the z-axis and one point in the x-y-plane to the central point due to the symmetry of the setup. In the experiment the size of the atom cloud is determined by an optical dipole trap. The typical spread for the planned setup is given by a distance

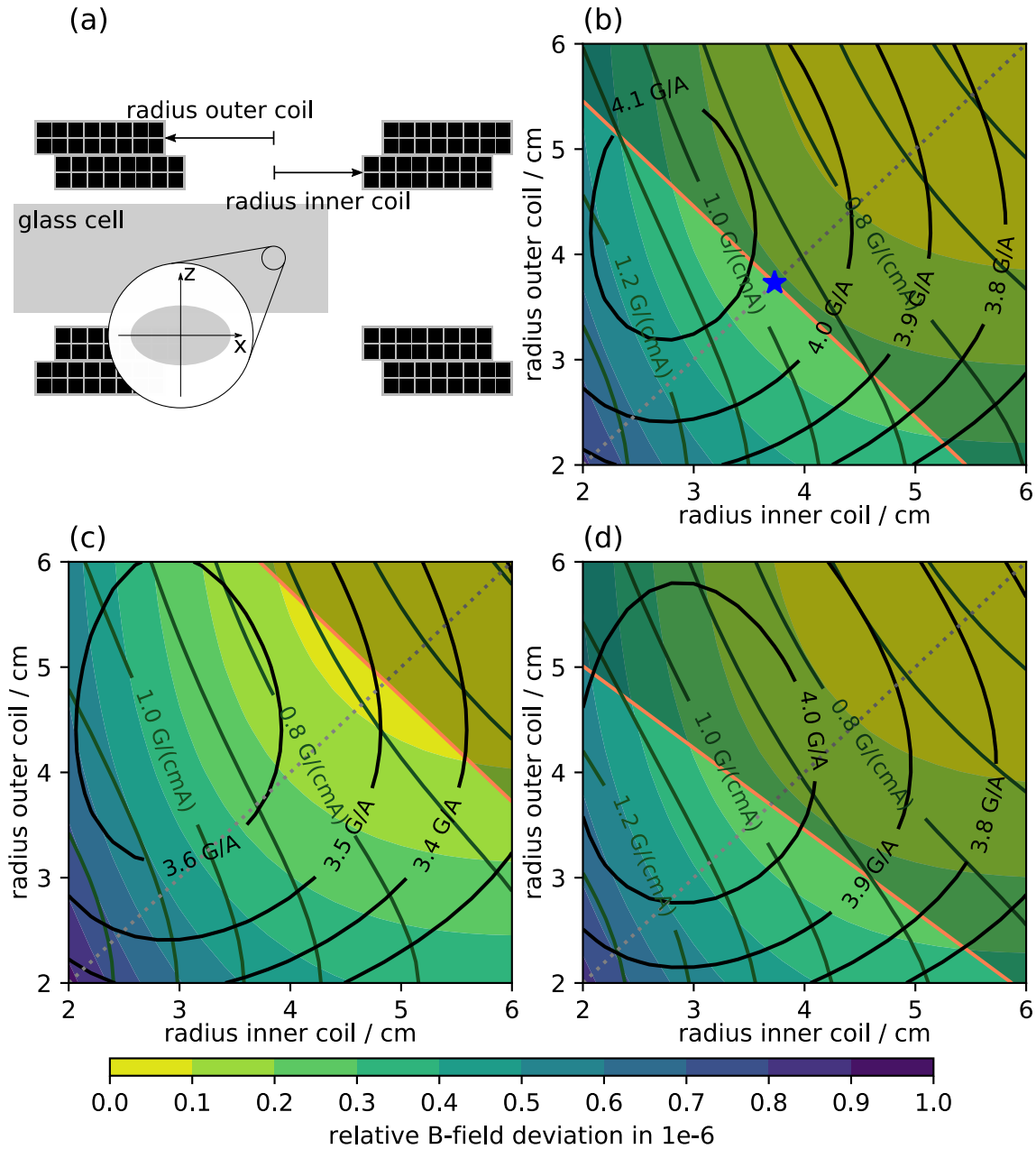


Figure 4.1.: Characterisation of different multicoil configurations. In (a) the cross section of the double-pancake coils in x-z-plane for eight windings each is depicted. The results of the numerical integration are shown in (b) for the case of eight windings each, in (c) for seven windings each, and in (d) for seven and nine windings for inner and outer double-pancake coils, respectively. The deviation of the magnetic field from the origin in the Helmholtz operation mode as defined in Equation 4.2 is colour-coded and the absolute field strength at the origin is plotted in black lines. For the gradient field operation mode the gradient along the strong z-axis at the origin is depicted in dark green lines. Additionally the upper bound of the coil size due to current source limitations is marked with a red line and a dashed grey line is added as a guide to the eye for equal coil radii. The final choice is depicted with the blue star.

of 30 μm from the centre in z-direction and 50 μm in x-direction. This is incorporated in the calculation and hence the maximal relative deviation of the magnetic field in the region of interest is

$$\delta_{\text{max}} = \max \left(\left| \frac{B(z = 30 \mu\text{m})}{B(0)} - 1 \right|, \left| \frac{B(x = 50 \mu\text{m})}{B(0)} - 1 \right| \right), \quad (4.2)$$

where B is the absolute field at the origin and at a point shifted in one direction, respectively. In this configuration the leftover free parameters are the inner radii of the coils. For symmetry reasons the radii of the two inner and the two outer coils are kept equal (cf. Figure 4.1 (a)) and were each varied between 2 cm and 6 cm with a resolution of 2 mm. For every configuration the absolute field in the centre and the deviation δ_{max} were calculated for the Helmholtz-like case. Additionally, the strength of the gradient at the centre was calculated in the Anti-Helmholtz case.

All these information are plotted in Figure 4.1 for double-pancake coils with eight windings each (b), seven windings each (c), and seven and nine windings for inner and outer coils, respectively (d). Many more configurations were simulated, but these were the most promising ones. Additionally to the above named quantities a grey dashed line is drawn as a guide to the eye for the case of equal radii for inner and outer coils. Also, as mentioned above, the power of the current source sets an upper bound to the length of the coils for reaching the maximum current. This bound is indicated by the red line and the coil radii have to be smaller in order to reach a current of 440 A.

Taking a closer look at the deviations reveals that they all become small in the upper right corner of the plots at radii above 5 cm. This roughly fits the Helmholtz criterion since taking into account the extend of the coils the mean distance between the coils is 7 cm and the mean radius is about 2 cm larger than the plotted inner radius of the coils. One has to keep in mind, though, that the deviation on the x-axis is incorporated as well, which shifts the optimal radius. To find the best configuration one can first look at the homogeneity. All configurations show similar behaviour in the deviation δ_{max} on the addressed scale. Configuration (d) is therefore not advantageous, since it is quite similar to (b) but would be more complicated in production as inner and outer coils have different winding numbers. This leaves (b) and (c). To gain homogeneity one has to choose rather large radii which is only possible in configuration (c). However, this would also lower the accessible absolute field and gradient strength. Comparing configurations (b) and (c) for equal coil radii (dashed line) at the boundary (red line) for 440 A the absolute field strength is about 1800 G and 1500 G, respectively. While this is not too much of an issue, the reachable gradient would drop by about 30 % from roughly 440 G/cm to 300 G/cm. To keep the ability for decent magnetic trapping and since the level of homogeneity is still rather high, configuration (b) with eight windings for each coil was favoured. Additionally equal radii for inner and outer coil were chosen to keep the production and the installation of the coils in the experiment as simple as possible. The radii were therefore set to be equal the intersection point of the grey dashed and the red line in (b), which leads to $r = 3.7$ cm (blue star in (b)).

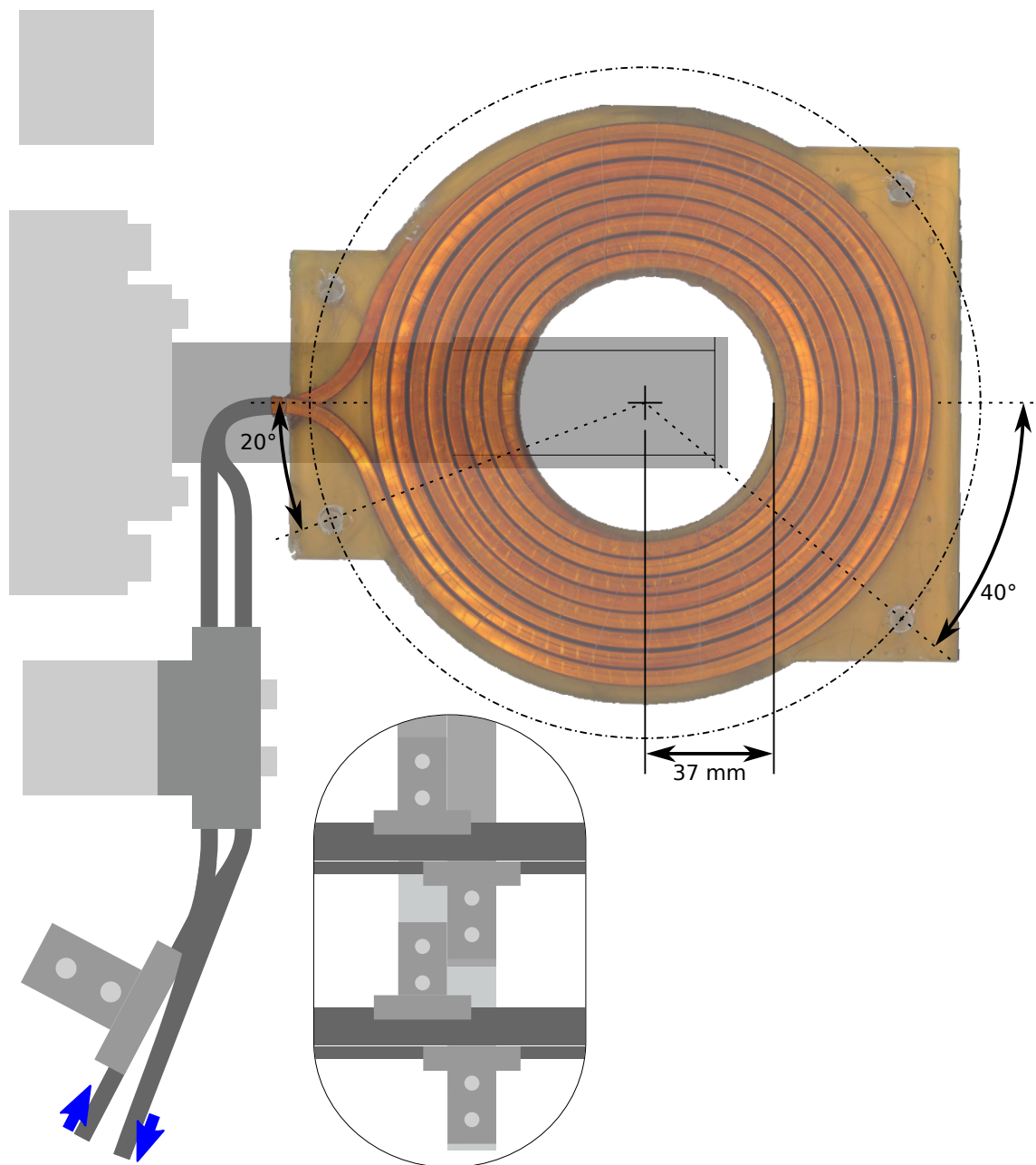


Figure 4.2.: Picture of one multicoil with a drawing of glass cell and wiring. The coil is vacuum casted in resin which is stabilised with glass fibre fabric. The inner radius is 37 mm, though one can see that the actual inner radius of the coil is bigger by about 2 mm. The glass cell is shown with the extension of its walls and the connecting flange. One can see that the holes for the front posts are in the blind spot of the optical contact area of the glass cell's front plate. Moreover the wiring is shown. The connection of copper hollow wire to the copper bars is shown in the inlay. The copper bars are mounted on the Item posts (grey squares). The two upper and lower coils, respectively, are connected to each other to form one coil as shown in the lower left corner. The hollow wire is connected to the cooling water system as depicted with the blue arrows.

4.2. Setup in the experiment

One of the coils with a sketch of the glass cell, wiring and relevant dimensions is shown in Figure 4.2 (technical drawing in section A.1). They were produced by the company Oswald. The coils were vacuum casted in resin (Araldit F) after the winding process. Glass fibre fabric was added to the resin to provide more stability and the resin itself should be stable up to temperatures of about 90 °C [35]. The finished coils are each 13 mm thick and have a inner radius of 37 mm. One can see, though, that this is not the actual inner radius of the coil which is about 2 mm larger. The position of the trapping region is determined by the position of the magnetic coils. It was chosen to be 15 mm from the sides of the glass cell and 20 mm away from the front plate. The position of the holes for mounting the coils on posts were chosen such that the front posts would stand in the blind spot which is created due to the optical contact process at the edges of the glass cell by the glass' finite thickness. The mounting was done with brassen posts that got produced by the institute's workshop. They are isolated from the optical table with Kapton tape to inhibit induction of currents when the magnetic fields are ramped up or down.

The first part of the wiring at the coils is done with 1 cm × 2 cm copper bars. The connectors to the coils were build in the institutes workshop (cf. section A.3) and soldered to the coils. The connectors feature a groove to increase the contact area to the coil wire leading to a low contact resistance. It was measured to be $R_c = 7.5 \mu\Omega$ which corresponds to a voltage drop of only 3 mV at 400 A. The copper bars are attached to the Item construction that holds the experiment and lead the current to the top of the housing of the experimental table (cf. Figure 4.2). Further wiring is done with 185 mm² copper stranded wire. It connects the coils with the current source which is located in the adjacent room. It is planned to use a bridge circuit to change between gradient and homogeneous operation mode and a passbank for regulation purposes (cf section 4.4). A current transducer (LEM IT 400-S) will be built in to measure the current. The planned setup is shown in Figure 4.3 The total length of the copper wire used is 10 m which amounts to a resistance of 0.93 m Ω and the copper bars are 4 × 1.3 m long leading to a resistance of 0.44 m Ω . At 440 A this leads to a voltage drop of 0.6 V. Hence a sufficient voltage should be left over to drive the passbank and the bridge circuit.

As mentioned above, the multicoils are water cooled in order to get rid of the heat. At 440 A the heating power of the coils is about 5.2 kW and has to be transported away. To reach a high level of stability a big external water reservoir is connected with a Riedel chiller (6.5 kW cooling power) and stabilised at 19 °C. The chiller uses the institute's cooling water system to dissipate the heat and provides a water pressure up to 5 bar. After the pump two Honeywell water filter units are located to filter the water and regulate the pressure providing two water cycles with different pressure. A sketch of the cooling system is shown in Figure 4.4. To get a high throughput not only a high pressure is needed but also a sufficient pipe cross-section. The Gardena Superflex garden hose has proven itself to be a good and reliable choice and was hence used with a cross-section of 1/2 inch to pipe the cooling water to and back

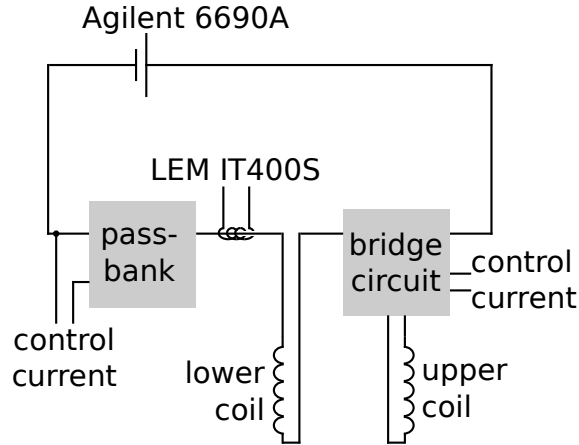


Figure 4.3.: Planned wiring of the multicoils. The coils are driven by a Agilent 6690A current source featuring an output of 440 A at 15 V. The current direction in the upper coil can be swapped with a bridge circuit depending on the operation mode of the coils. After the lower coil a LEM IT 400-S current transducer is used to measure the current flow and a passbank is build in for regulation purposes.

from the experiment. At the experiment it is then split up in four 6 mm plastic tubes that isolate the coils electrically and let the water to flow through the coils in parallel (cf. section A.4). This provides uniform cooling for all the coils. To reduce heat accumulation between the coils the flow direction of the water is set to enter each of the two stacked coils in the middle layers and leave at the upper and lower, respectively.

4.3. Performance

For the experiment it is important to check the performance of the multicoils. Since measuring on a 100 μm scale was not possible the coils were simulated. They were scanned with a flatbed scanner from both sides to capture both layers and were digitalised [36]. The two dimensional parameterisations were then merged by hand to a three dimensional model. The change of height between the two layers within one coil was included whereas the connections and further wiring was not included in this model. Using the same numerical integration method as above the magnetic fields were calculated for the homogeneous and the gradient field configuration with a resolution of 2 μm .

The centre of the homogeneous field exhibits a minimum in the gradient of the absolute magnetic field as homogeneity is maximal there. Around this central point the field was simulated in a box with 200 μm side length. An overview of the absolute field is shown in Figure 4.5. The resulting absolute field in the centre is

$$B(0) = 3.97 \text{ G/A}. \quad (4.3)$$

Further away from this central point in the x-y-plane the field slightly decreases as

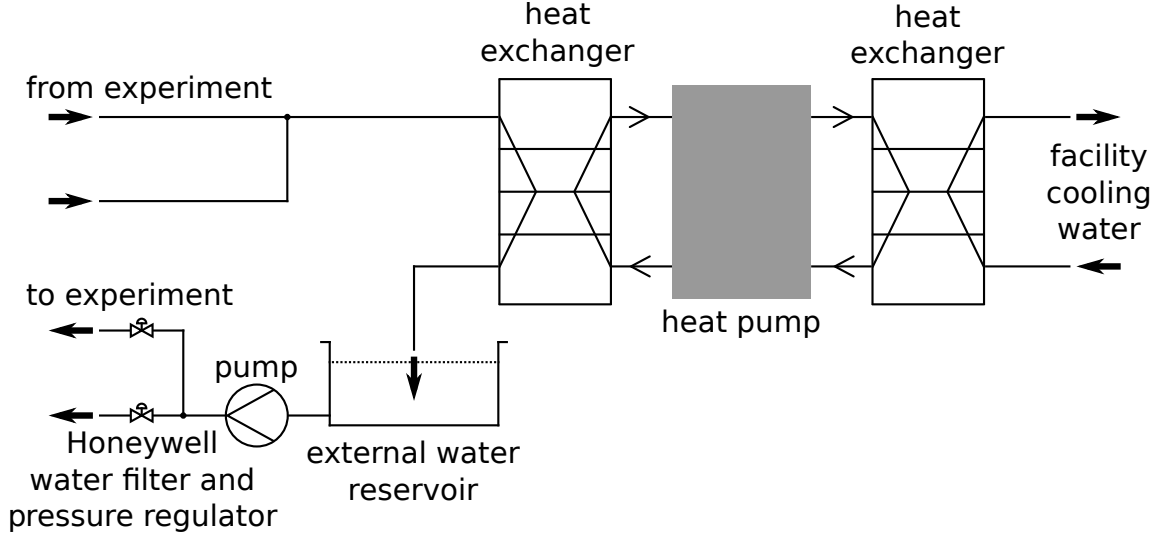


Figure 4.4.: Cooling system of the experiment. Additionally to the facility cooling water a more stable system was set up. It provides two water cycles at different pressure stabilised to 19 °C using a Riedel chiller with 6.5 kW cooling power to exchange the heat with the facility cooling water. Two Honeywell units support water filtration and pressure regulation.

it is shown in Figure 4.6 (a). The deviation of the magnetic field relative to the centre, $\delta(x) = B(x)/B(0) - 1$, is plotted. Only the x-axis is shown since the field is radially symmetric around the z-axis on the order of 10^{-7} . The ideal case of current loops which was used to find the optimal configuration is included in the plot as well and one can see that there is no major difference. The same holds for plot (b), where the deviation along the z-axis is shown. On this axis the field increases from the centre which indicates that the coils radius is smaller than the Helmholtz radius [36]. For both cases a polynomial of order two is fitted to the data of the real coils. The quadratic term is dominant in both cases and its parameters are $\beta_x = -7.44 \times 10^{-3} \text{ m}^{-2}$ and $\beta_z = 1.55 \times 10^{-2} \text{ m}^{-2}$. One can conclude that the field deviation around the centre is consistent with previous simulations and stays within the order of 10^{-6} . Also, the calculations showed that x- and y-components can be neglected as they are smaller by at least three orders of magnitude in the considered region.

Taking a look at the gradient configuration one can find the centre by searching for the minimum of the absolute magnetic field. This point will be the central point of the magnetic trap. Due to the non-uniform shape of the coils one finds that it does not overlap with the centre of the homogeneous field configuration but differs by

$$\mathbf{r}_{\text{grad}} - \mathbf{r}_{\text{hom}} = (408 \text{ } \mu\text{m}, 2 \text{ } \mu\text{m}, -277 \text{ } \mu\text{m}). \quad (4.4)$$

The gradients in the different directions yield

$$g_x = 0.44 \text{ G/cmA}, \quad g_y = 0.46 \text{ G/cmA}, \quad g_z = -0.91 \text{ G/cmA} \quad (4.5)$$

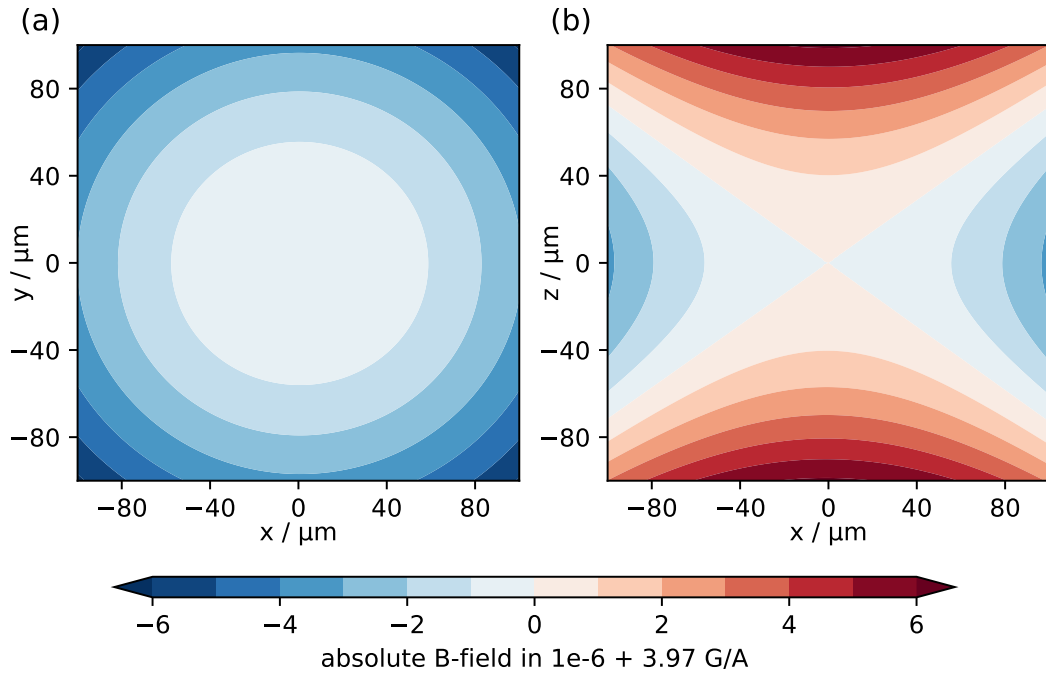


Figure 4.5.: Absolute homogeneous magnetic field around its centre. The field strength is colour coded where the field at the centre (3.97 G/A) is set to neutral colour. In (a) the field in the x-y-plane exhibits a maximum at the central point. In (b) the field in the x-z-plane is shown which grows in the z direction as one approaches the magnetic coils. On the plotted scale the field in the x-z-plane is radially symmetric around the z-axis on the order of 10^{-7} .

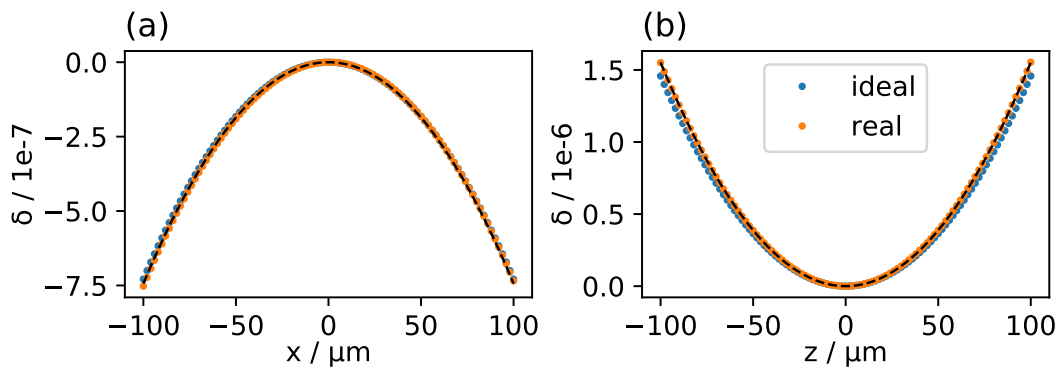


Figure 4.6.: Relative deviation of the magnetic field of the multicoils. The field got simulated on the axes through the centre of the homogeneous magnetic field for the ideal case (current loops) and the real parametrised coils. The deviation relative to the central point on the x-axis is shown in (a), on the z-axis in (b). The result for the y-axis is not shown since it matches the x-axis result. The deviation for the parametrised coils is fitted by a polynomial of order two and leads to $\beta_x = -7.44 \times 10^{-3} \text{ m}^{-2}$ and $\beta_z = 1.55 \times 10^{-2} \text{ m}^{-2}$. The plots show that both simulations match well.

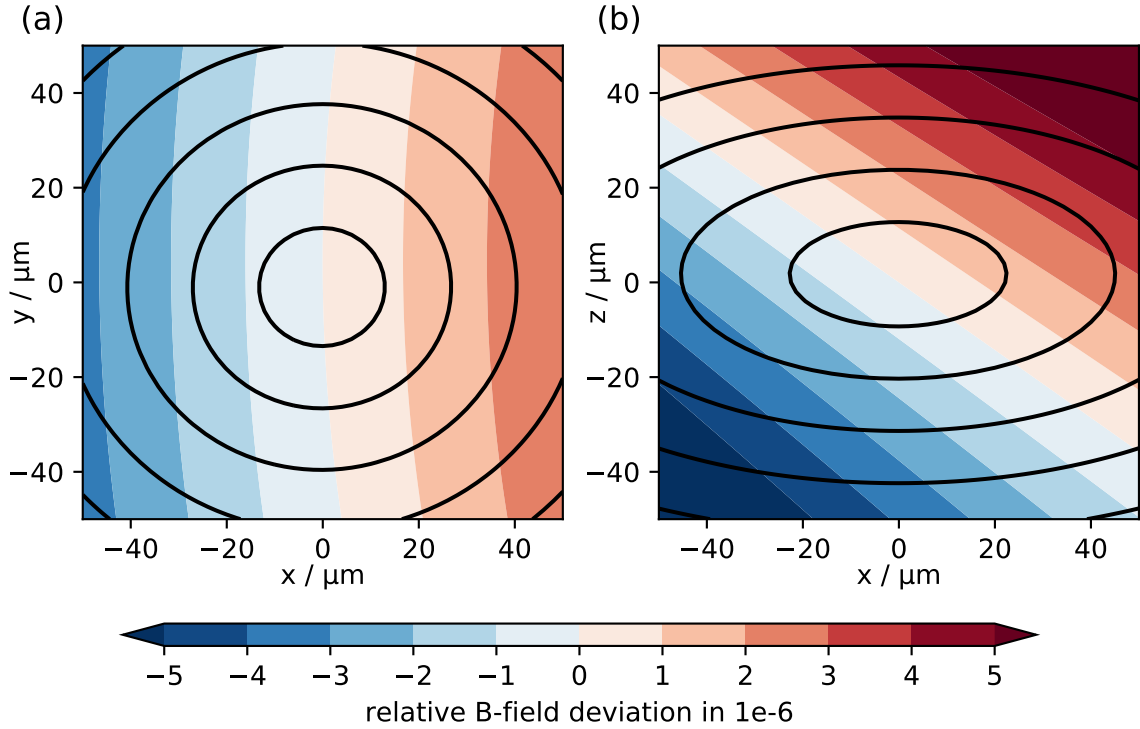


Figure 4.7.: Deviation of the homogeneous magnetic field from its value at the gradient field centre. The equipotential lines of the magnetic trap are included as a guide to the eye. The magnetic field maintains a rather high level of homogeneity as it only changes by roughly 6×10^{-6} over the plotted range. The deviation in y-direction is negligible since the central points of the two field configurations are not shifted in this direction.

at the central point. They only change on the order of 10^{-3} on the z-axis and one order of magnitude less in the x-y-plane over a range of 2 mm around the central point.

The fact that the central points of the homogeneous and the gradient field do not overlap can cause problems in the experiment. Whereas the early stages of the experiment such as the MOT are performed around the centre of the gradient field, one needs a homogeneous field for tuning the scattering length during the late stages of the experimental sequence. To evaluate the severity of this the deviation of the homogeneous magnetic field from its value at the gradient field centre is plotted in Figure 4.7. As a guide to the eye lines of equal magnetic gradient field are included, which represent the equipotential lines of the magnetic trap. Over the plotted range of $100 \mu\text{m}$ the field changes by roughly 6×10^{-6} which still is a rather high level of homogeneity. Furthermore one can see that this deviation mainly occurs in x- and z-direction since the centre point is not shifted in y-direction.

As a next step the connections of the coils with the copper bars and the bars themselves were added to the simulation. They merely lead to a shift of the field and

therefore affect the central points. Calculating the distance between the centres one gets

$$\mathbf{r}_{\text{grad}} - \mathbf{r}_{\text{hom}} = (508 \mu\text{m}, 3 \mu\text{m}, -295 \mu\text{m}) \quad (4.6)$$

with wiring, which is larger than before and shows that predominantly the x-direction is affected. To match the two central points one could add an offset field to the gradient field to shift the point of zero magnetic field. Assuming a constant gradient one would need to add a field of 2.2 G per 100 A multicoil current in x-direction and 2.7 G per 100 A in z-direction. The necessary field is within the operation range of the offset coils developed in [36] and can therefore be easily implemented.

4.4. Passbank

Since the built-in regulation of the current source is too slow for the desired magnetic field ramps an external regulator is needed. This is commonly done with a *passbank* consisting mainly out of transistors connected in parallel.

To allow for switching currents up to 440 A bipolar Darlington power transistors are used in parallel. They contain two bipolar transistors in a row to allow for switching of higher currents. The model ON MJ11032G was used since good experiences were made with it. Its maximum continuous collector current rating is 50 A hence it was decided to run the passbank with 20 transistors in parallel. This exposes the single transistor to a current of maximal 22 A and ensures safe operation of the transistors.

When using transistors in parallel one has to take care of the current flow through the different transistors since they usually have different DC current gains h_{FE} . To understand how this affects the current flow one can simplify the problem and look at two transistors connected in parallel (cf. Figure 4.8). The LED and the resistor are neglected at first. When the driving voltage U_{D} gets higher, the transistors become active. However, the exact voltages differ from transistor to transistor. Therefore one transistor becomes active first carrying more current than it can handle. This effect is called *current hogging* [37].

Even if all transistors would become active at the same time another effect must be taken into account. Depending on the base-emitter current I_{BE} an emitter current of $I_{\text{E}} = h_{\text{FE}} I_{\text{BE}}$ flows which highly depends on the gain. As the gain varies from transistor to transistor one of them has to carry a higher load and heats up more. Since the resistance of bipolar transistors decreases with rising temperature, even higher currents flow through the transistor and it has to carry even more load. This is called *thermal runaway* [37] and could easily destroy the transistors one after the other.

To prevent both effects and ensure an even current distribution a resistor is placed after the transistor. It provides a voltage drop U_{R} and therefore acts as a negative feedback loop as the driving voltage is split between the transistor and the resistor, $U_{\text{D}} = U_{\text{BE}} + U_{\text{R}}$. If the emitter current I_{E} rises the voltage drop U_{R} increases. Hence the base-emitter voltage U_{BE} has to decrease leading to a lower emitter current I_{E} .

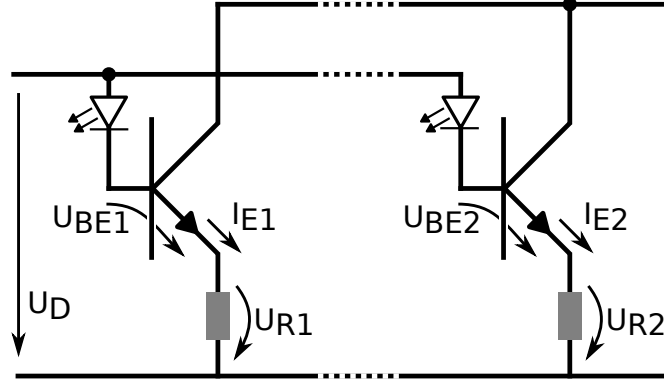


Figure 4.8.: Simplified sketch of the passbank circuit. The passbank consists of 20 bipolar darlington power transistors (MJ11032G) connected in parallel of which two are shown in this sketch. A diode is added on the base side to provide a safety device in case a transistor breaks down and to work as an optical feedback for the performance of the transistor. At the emitter side a negative feedback for the control current is implemented using a $2\text{ m}\Omega$ resistor.

To describe this process and get a rough estimate for the necessary resistor the Ebers-Moll model [37] can be used. Depending on the base-emitter voltage U_{BE} it describes the emitter current

$$I_E = I_S \left(e^{\frac{U_{BE}}{U_T}} - 1 \right), \quad (4.7)$$

where U_T is the thermal voltage ($k_B T/q \approx 26\text{ mV}$ at room temperature $T \approx 300\text{ K}$ with k_B the Boltzmann constant and q the electron charge) and I_S the saturation current of the particular transistor. Looking at the simplified system in Figure 4.8 both transistors share the same driving voltage U_D , leading to

$$U_{BE1} + U_{R1} = U_{BE2} + U_{R2}. \quad (4.8)$$

Using Equation 4.7 and $U_R = RI_E$ to replace the voltages in Equation 4.8 one gets

$$U_T \ln \left(\frac{I_{E1}}{I_{S1}} \right) - RI_{E1} = U_T \ln \left(\frac{I_{E2}}{I_{S2}} \right) - RI_{E2} \quad (4.9)$$

$$\Rightarrow R = \frac{U_T}{I_{E1} - I_{E2}} \ln \left(\frac{I_{E1} I_{S2}}{I_{E2} I_{S1}} \right) \approx \frac{U_T}{\Delta I_E}. \quad (4.10)$$

As the two emitter currents I_E and the two saturation currents I_S are roughly the same, the logarithm can be neglected. This leaves a resistance which is dependent on the desired emitter current difference ΔI_E that is a measure for the stability of the system. Equation 4.10 shows that the system becomes more stable with a bigger resistor as the emitter current difference ΔI_E is lower. On the downside a bigger resistor will lead to a higher power dissipation.

In the following the size and type of the resistor has to be determined. The transistors each carry a load of about 20 A. To ensure the transistors stay within safe operation mode a maximal current difference of $\Delta I_E = 15$ A was chosen. With Equation 4.10 this leads to a resistance of

$$R = 1.73 \text{ m}\Omega. \quad (4.11)$$

As the resistor has to endure currents of about 20 A, it was decided to make it from a wire. A piece of 10 cm copper wire with 1 mm diameter was successfully tested. It has a resistance of 2.3 m Ω and hence adds some extra stability.

Additionally LEDs are added to the base of the transistor. They serve as a safety device if a transistor breaks down. It was discovered that a breakdown can destroy the collector-base diode of the transistor. This allows the collector current to flow out of the base of the broken transistor and act as base-emitter current for the still working transistors. In this case all the other transistors become fully active and the passbank is not controllable anymore. The diode prevents this scenario and gives optical feedback in case a transistor broke and the base-emitter current is interrupted.

Another important design question is how to dissipate the heat produced by the transistors due to the high currents. Passive cooling is not sufficient and hence the passbank has to be cooled actively. The transistors used feature the TO-3 package and therefore provide a large contact area for heat dissipation. They are arranged on a copper block which serves as collector contact and heat sink for the transistors. On its back two 6 mm copper tubes are soldered into grooves to ensure good thermal contact for cooling. For cooling the facilities' cooling water is used. The technical drawings can be found in section A.2.

5. Characterisation of the ^{39}K MOT

Alongside the installation of the magnetic coils a laser system for potassium was set up [33]. Furthermore the optomechanics for the 2D and 3D-MOT were implemented, where the 2D-MOT serves as a source of cold atoms to load the 3D-MOT. After optimisation a ^{39}K MOT could be observed and is shown in Figure 5.1.

For optimisation purposes and later experiments it is important to characterise the performance of atom source and MOT, namely how fast the atom source can load the MOT and how many atoms can be captured in the MOT. This was done using fluorescence imaging. The MOT was directly imaged on the power meter with one lens (cf. Figure 5.2) and a fraction of the light emitted by the trapped atoms is measured.

To conclude the trapped number of atoms, one has to calculate the power P_{atom} that is emitted by one atom into the observed solid angle Ω . As the energy of a single photon is hc/λ and the atom emits photons with the rate γ_{sc} , one gets

$$P_{\text{atom}} = \frac{hc}{\lambda} \gamma_{\text{sc}} \Omega. \quad (5.1)$$

The emission rate γ_{sc} , which is equal to the scattering rate for an atom in a steady state, is given in Equation 2.2 and depends on the transitions' spontaneous emission rate γ as well as the detuning δ and saturation parameter s of the incident trapping light.

The spontaneous emission rate was taken to be the average of the D1 and D2 line of ^{39}K , $\gamma = 2\pi \cdot 6 \text{ MHz}$ [19], since both lines contribute equally. The detuning of the trapping light was measured to be $\delta = 12 \text{ MHz}$. The saturation parameter s describes the intensity relative to the saturation intensity, $s = I/I_s$ (cf. Equation 2.1). The saturation intensity amounts to $I_s = 1.75 \text{ mW/cm}^2$ [19] for the considered transitions.

To calculate the saturation parameter s one has to determine the trapping light intensity first. Since the trapped atom cloud is much smaller than the beams the mode profile of the beam has to be taken into account. The light intensity is higher in the central region of the beam where the atom cloud is located. Assuming a gaussian mode, the radial beam profile can be described by

$$A(\rho) \sim \exp(-2\rho^2), \quad (5.2)$$

where $\rho = r/r_0$ is the normalised radius and r_0 is the $1/e^2$ radius of the considered beam. The diameter of the MOT beams is 14 mm [33] and their power was measured to be 32 mW in total. In contrast the estimated diameter of the MOT is only 3 mm.

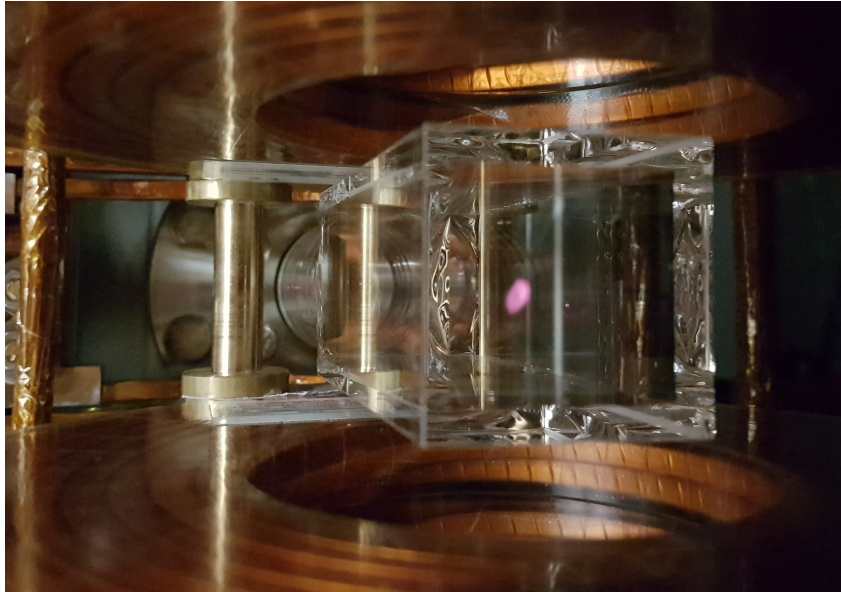


Figure 5.1.: Picture of the potassium MOT. The picture was taken with a smartphone. This leads to a shift of the colour of the atom cloud due to infrared light captured by the camera as well.

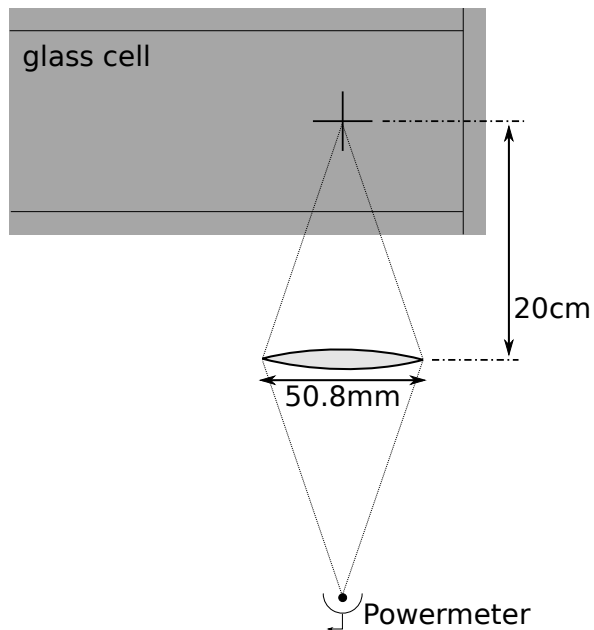


Figure 5.2.: Fluorescence measurement of the trapped atom cloud (not to scale). A lens is used to focus the atom cloud onto a powermeter which reads out the intensity of the fluorescence.

Assuming the atom cloud to be round and in the middle of the beams, the fraction f of the light reaching the atoms can be estimated by comparing the integrated profile

$$f = \int_0^{\rho_{\text{MOT}}} A(\rho)\rho d\rho / \int_0^\infty A(\rho)\rho d\rho, \quad \text{with } \rho_{\text{MOT}} = r_{\text{MOT}}/r_0. \quad (5.3)$$

The integration over the angular part cancels and only the radial part is left over. Inserting the measured values from above one gets

$$\rho_{\text{MOT}} = 1.5 \text{ mm}/7 \text{ mm} = 0.21 \quad \Rightarrow f = 8.4 \%. \quad (5.4)$$

This means the power reaching the trapped atom cloud is 2.7 mW, corresponding to an intensity of 38 mW/cm². With the saturation intensity mentioned above a saturation parameter $s = 22$ can be calculated. Putting everything together the scattering rate is

$$\gamma_{\text{sc}} = 0.56 \frac{\gamma}{2} = 2\pi \cdot 1.68 \text{ MHz}. \quad (5.5)$$

Next, the solid angle Ω has to be determined. It is assumed, that the emitted photons are distributed equally in all directions and can reach the first lens without loss. Also, all photons reaching the first lens are considered to reach the detector as well. The solid angle is therefore determined by the quotient of the area covered by the first lens and the surface of the sphere at its distance,

$$\Omega = \pi r_{\text{lens}}^2 / 4\pi D_{\text{lens}}^2, \quad (5.6)$$

where r_{lens} is the radius of the lens and D_{lens} its distance to the atom cloud. The calculation gives $\Omega_{\text{B}} = 4.0 \times 10^{-3}$.

Summing up, the atom numbers can be calculated. For the fully loaded trap a power of $P_{\text{B}} = 2.6 \mu\text{W}$ was measured. This leads to an atom number of

$$N = \frac{P_{\text{B}}}{P_{\text{atom, B}}} = \frac{2.6 \mu\text{W}}{1 \times 10^{-14} \text{ W}} = 2.6 \times 10^8. \quad (5.7)$$

Furthermore the loading rate was estimated. After a loading the trap for 200 ms the fluorescence was measured to be 0.23 μW . This leads to a loading rate of

$$n = \frac{1.1 \mu\text{W/s}}{1 \times 10^{-14} \text{ W}} = 1.1 \times 10^8 \text{ 1/s}. \quad (5.8)$$

This result shows on one hand that the performance of the source could be optimised further, as similar experiments show loading rates in the order of 10^{10} 1/s [38]. This is, however, strongly depending on the pressure in the 2D-MOT chamber and a better performance can be reached if one accepts worse vacuum conditions in the experimental chamber. On the other hand, the performance is sufficient for further experimental steps towards a BEC.

6. Conclusion and Outlook

This thesis gives an overview of the experimental system of the newly designed potassium BEC experiment. First the vacuum system and the laser setup were shown shortly. Afterwards the design requirements for magnetic field coils were discussed and a simulation was done to find the best configuration. Two pairs of double-pancake water-cooled coils with a radius of $r = 3.7$ cm were chosen. Then the setup of the coils in the experiment and the supply systems were described with a focus on the current control with a passbank. Finally the magnetic coils were simulated with their actual geometry to estimate their performance. For the homogeneous field a strength of 3.97 G/A was found and within a region of ± 100 μm around the centre the deviation was calculated to be less than 1.5×10^{-6} . The gradient field reaches 0.91 G/cmA on the strong axis. Simultaneously the laser system was set up [33]. After optimisation of the system a potassium MOT could be observed. Its particle number was estimated to be 2.6×10^8 with a loading rate of 1.1×10^8 1/s.

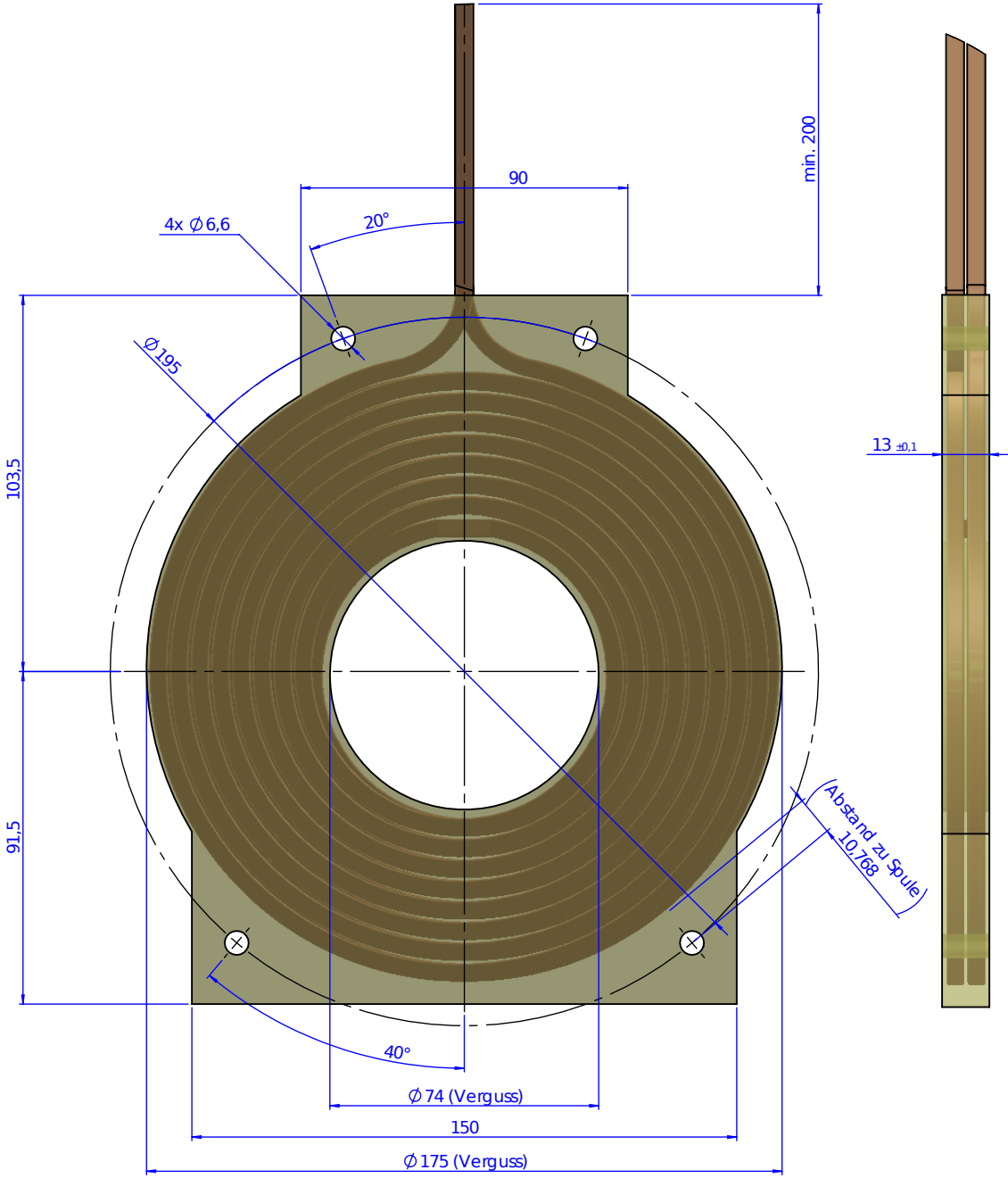
To advance on the route to a BEC the grey molasses cooling scheme will be implemented next. This allows for sub-doppler cooling of the ^{39}K MOT. The necessary D1 laser system is implemented already. For optimisation of the MOT and grey molasses an absorption imaging system will be set up. If the cooling process is adjusted properly and low enough temperatures can be reached the atom cloud is loaded into an optical trap. The trap will be generated by a 50 W solid-state laser, which was purchased already. If direct loading into the optical trap is not possible, a phase of magnetic trapping will be put in between. In both cases further cooling will take place with the help of forced evaporation. As discussed above it is necessary to tune the scattering length when going to lower temperatures. A broad Feshbach resonance exists in the $F = 1$, $M_F = 1$ ground state and can be used. The tuning can only be done in the optical dipole trap, so the atoms should be loaded in the dipole trap as soon as possible. Changing the scattering length enhances the evaporation process and prevents the condensate from collapsing. Finally, quantum degeneracy can be reached.

The broad Feshbach resonance of ^{39}K allows for tuning the atomic interaction and hence gives access to many physical regimes. An interesting research direction could be the dynamics of systems far from equilibrium. This regime can be reached by a quench of an experimental parameter such as the scattering length. It is achieved by inducing a spin-flip or changing the magnetic field in the vicinity of a Feshbach resonance. After an evolution time the state of system can be measured, for instance, the spatial density variation. Also, the momentum distribution can be determined well after time-of-flight of the atomic cloud as the system can be tuned to a non-interacting regime. These observables allow for conclusions about the dynamics of the system.

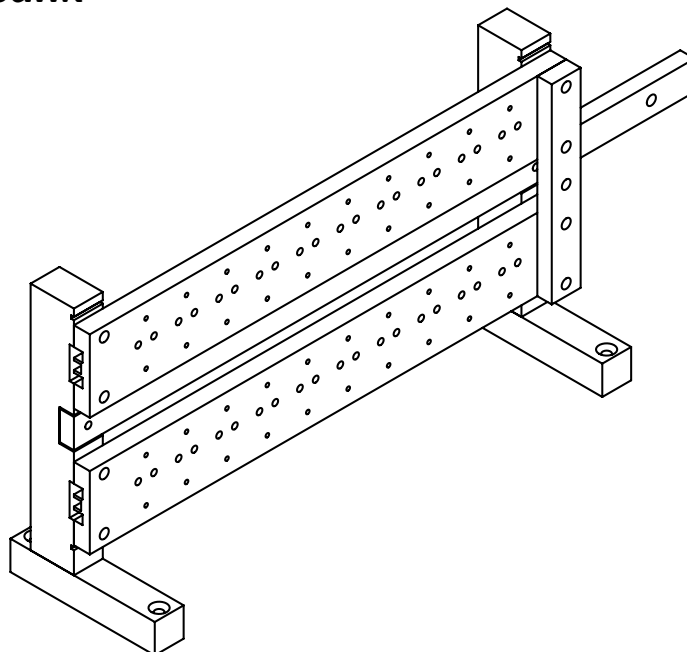
Summing up, this setup provides a versatile system for the study of many-body quantum dynamics, for example in the vicinity of non-thermal fixed points [39].

A. Technical drawings

A.1. Multicoils



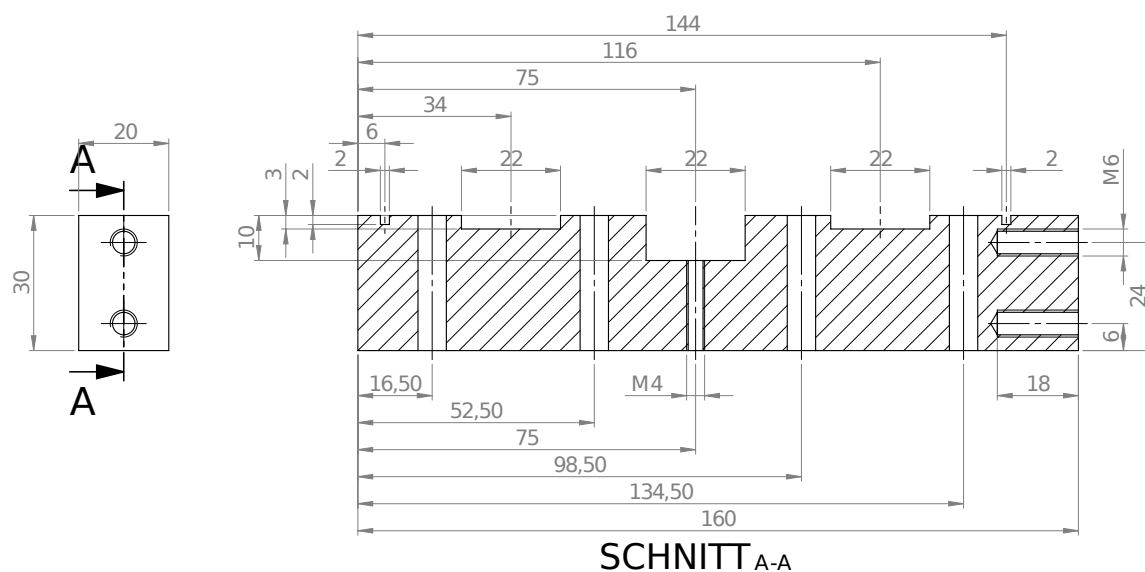
A.2. Passbank

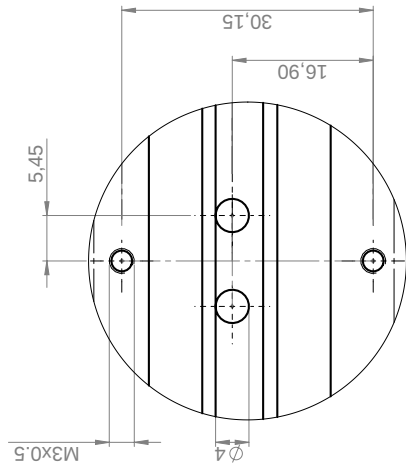
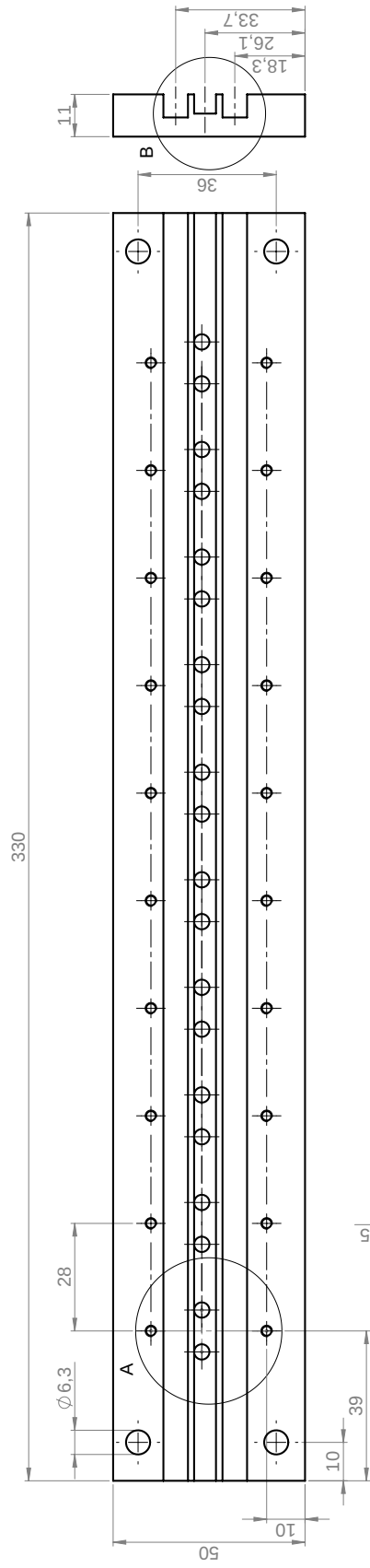


The above drawing shows the passbank without electrical components and cooling system. The two big copper plates feature holes and threads for the transistors and grooves on the back. The two outermost are used to solder in copper tubing for cooling and the inner groove simplifies the soldering of the transistors. On the front side the transistors are placed. The copper plates work as heat sink and are connected to the collector of the transistor. A detailed sketch is shown on the opposite page.

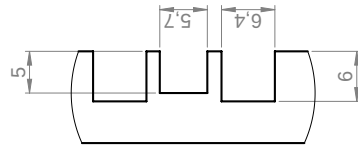
The copper bar in the middle collects the emitter currents. Short copper wires with 3 mm diameter were soldered to it using a blowlamp. This allows to easily attach further wiring with a soldering iron. The emitter side of the transistors is connected to the central copper bar using a thin wire that acts as a resistor (cf. section 4.4).

Below a sketch of the holder is shown.



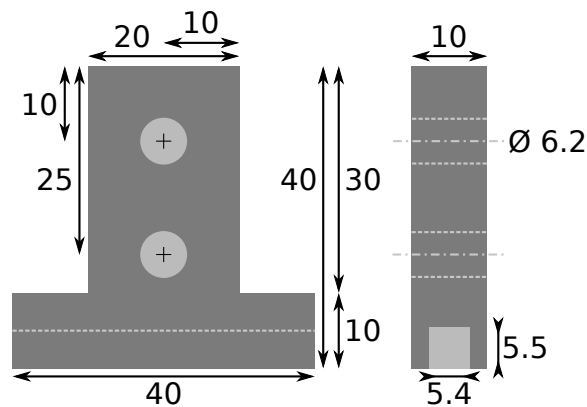


DETAIL A
MAßSTAB 2 : 1

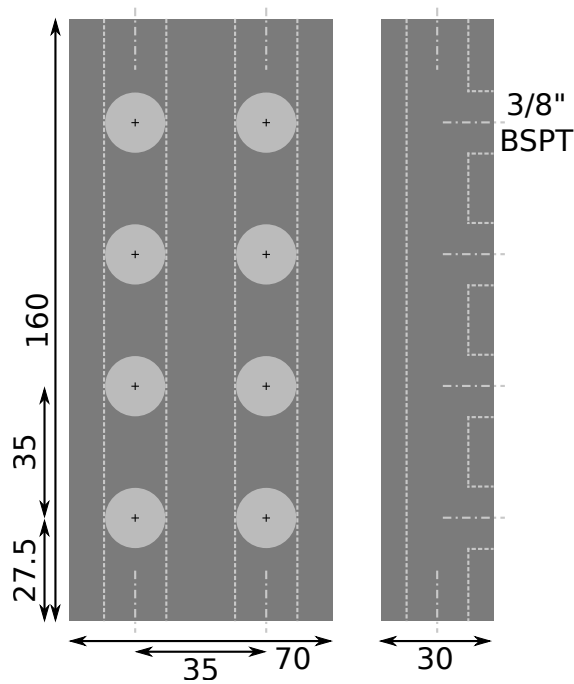


DETAIL B
MAßSTAB 2 : 1

A.3. Current connector

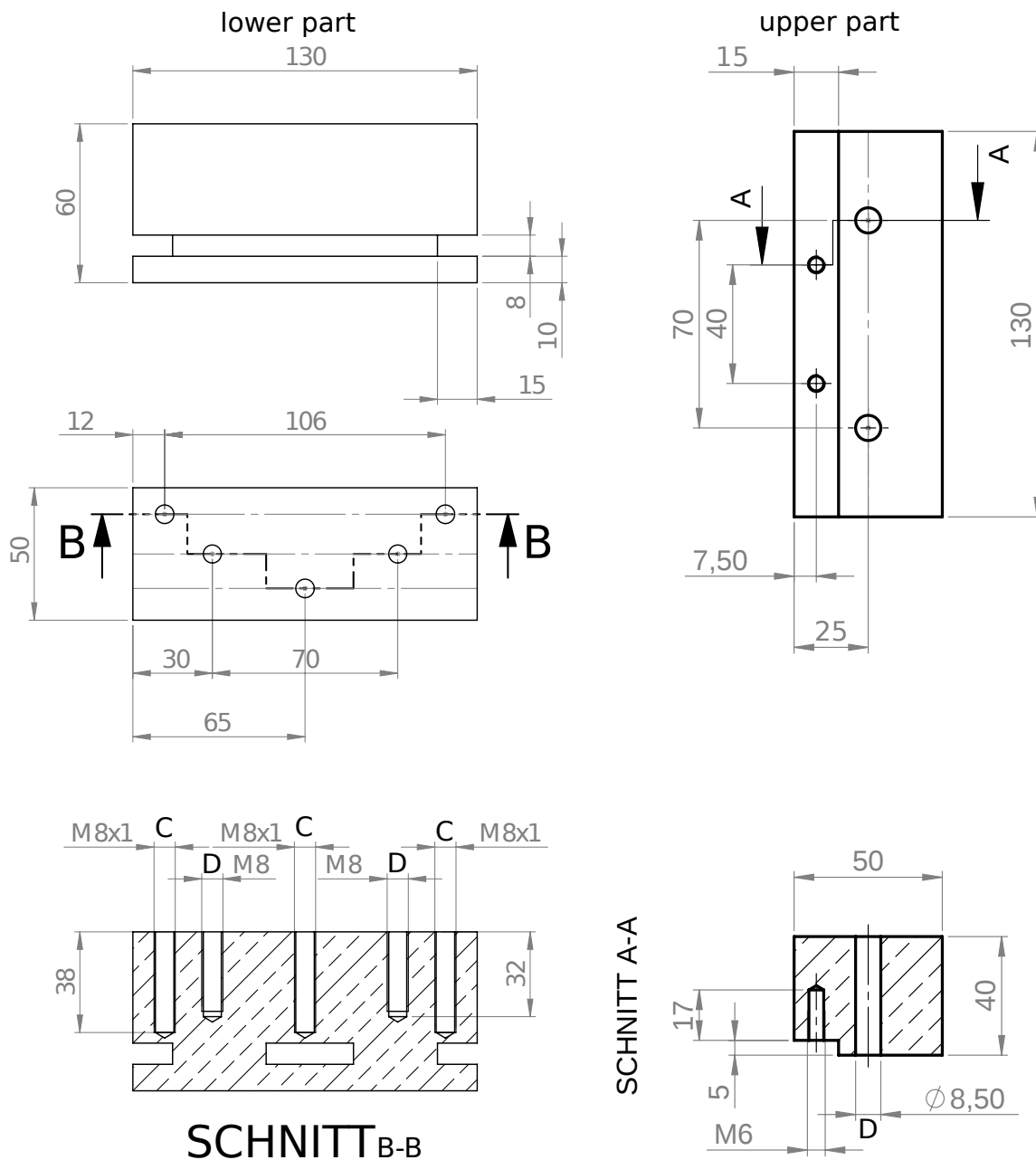


A.4. Water splitter



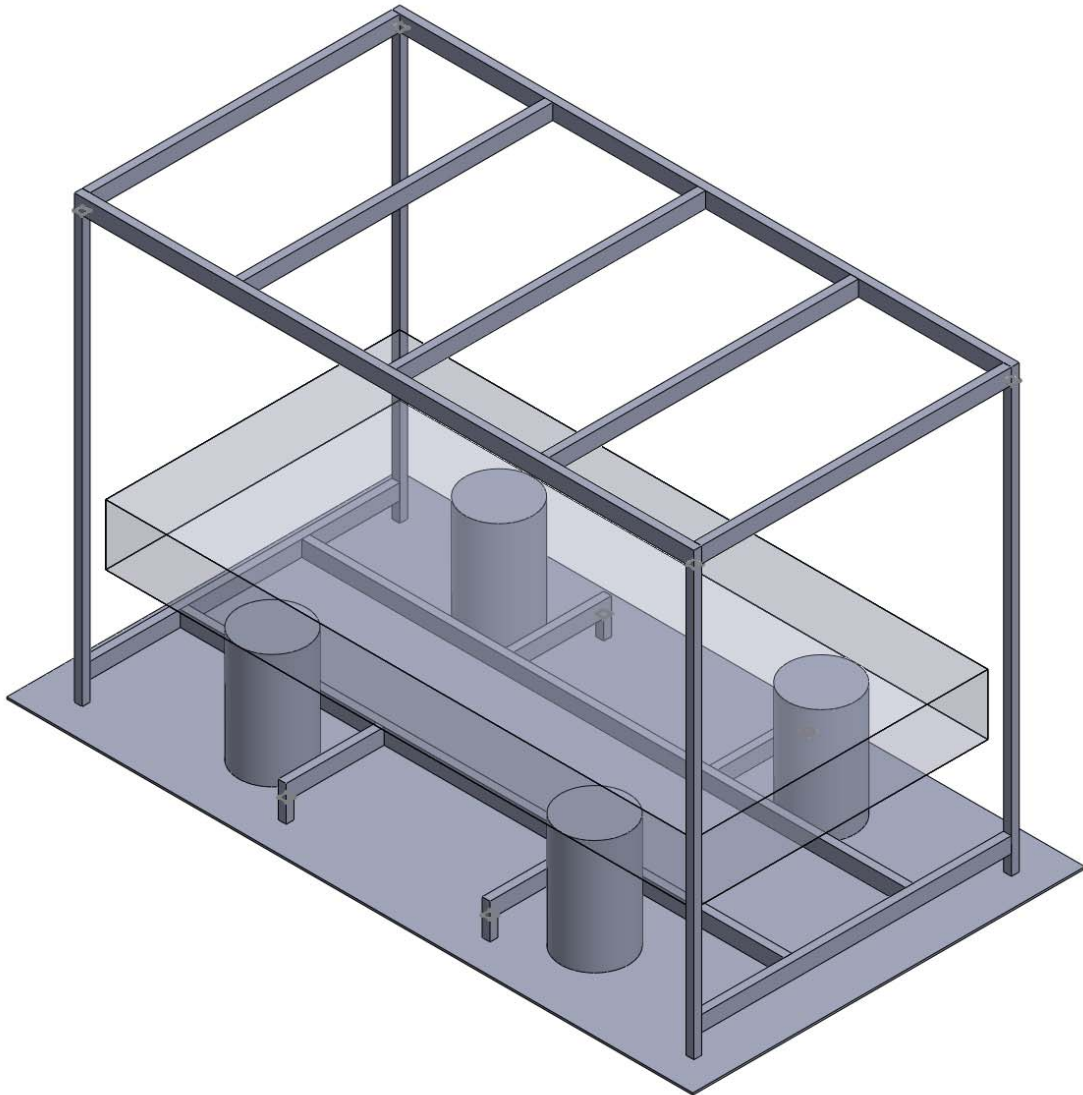
The above drawing shows the water splitter. From the upper left/right water streams in/out and is divided into four pipes. All the holes were manufactured 3/8" British Standard Pipe Thread (BSPT). The two ports on top were equipped with hose connectors and the opposite two ports were closed with blind plugs. The front ports were all equipped with connectors for 6 mm tubing. The author would like to emphasise the importance of thread standards as there exist many. Especially, one should not confuse male BSPT with male NPT (National Pipe Taper) that are quite similar, but still not the same.

A.5. Holder for vacuum chamber



To stabilise the vacuum chamber on the table it was fixed on the table at the two big flanges of the experimental chamber (cf. Figure 3.1). It consists of two parts. The upper part is connected to the flange with an aluminium collar. The lower part is clamped to the optical table. The upper part sits on three adjustment carriage bolts (in threads C) with a 19 mm head and is then secured with two Allen screws (in threads/clearance holes D).

A.6. Housing for optical table



The housing for the optical table is built from Item aluminium profiles. As shown in the picture above it is freestanding to avoid vibrations on the optical table. On top it is closed with wooden multiplex boards (21 mm thick) and around the table opaque curtains ensure laser safety. Below the optical table multiplex boards are put on the Item construction and provide further space to place equipment off the ground.

B. Numerical integration scheme

The numerical integration scheme shown in Equation 4.1 was implemented with the help of python.

```
def GetVecB(r, coils):  
    """Calculate B-field vector at r for list of coils  
    """  
    v = np.zeros(3)  
    for c in coils:  
        for i in range(len(c)-1):  
            dl = c[i+1]-c[i]  
            v += (np.cross(dl,c[i]-r)/(sum((c[i]-r)**2)**(3/2)))  
    result = 0.1*v  
    return result
```

For every point r this function calculates the magnetic field for a given set of coils. This set is saved in `coils`. In this variable all coils are represented by an ordered list of the points, that are the start- and endpoints of the discrete line elements Δl .

Bibliography

- [1] W. D. Phillips and H. Metcalf. *Laser deceleration of an atomic beam*. Phys. Rev. Lett. **48**, 596–599 (1982).
- [2] S. Chu, L. Hollberg, J. E. Bjorkholm, A. Cable, and A. Ashkin. *Three-dimensional viscous confinement and cooling of atoms by resonance radiation pressure*. Phys. Rev. Lett. **55**, 48–51 (1985).
- [3] M. H. Anderson, J. R. Ensher, M. R. Matthews, C. E. Wieman, and E. A. Cornell. *Observation of Bose-Einstein Condensation in a Dilute Atomic Vapor*. Science **269**, 198–201 (1995).
- [4] K. B. Davis, M. O. Mewes, M. R. Andrews, N. J. Van Druten, D. S. Durfee, D. M. Kurn, and W. Ketterle. *Bose-Einstein condensation in a gas of sodium atoms*. Phys. Rev. Lett. **75**, 3969–3973 (1995).
- [5] S. Inouye, M. R. Andrews, J. Stenger, H.-J. Miesner, D. M. Stamper-Kurn, and W. Ketterle. *Observation of Feshbach resonances in a Bose-Einstein condensate*. Nature **392**, 151–154 (1998).
- [6] C. Chin, R. Grimm, P. Julienne, and E. Tiesinga. *Feshbach resonances in ultracold gases*. Rev. Mod. Phys. **82**, 1225–1286 (2010).
- [7] H. Wang, A. N. Nikolov, J. R. Ensher, P. L. Gould, E. E. Eyler, W. C. Stwalley, J. P. Burke, J. L. Bohn, C. H. Greene, E. Tiesinga, C. J. Williams, and P. S. Julienne. *Ground-state scattering lengths for potassium isotopes determined by double-resonance photoassociative spectroscopy of ultracold ^{39}K* . Phys. Rev. A **62**, 52704 (2000).
- [8] M. Fattori, C. D’Errico, G. Roati, M. Zaccanti, M. Jona-Lasinio, M. Modugno, M. Inguscio, and G. Modugno. *Atom interferometry with a weakly interacting bose-einstein condensate*. Phys. Rev. Lett. **100**, 080405 (2008).
- [9] G. Roati, C. D’Errico, L. Fallani, M. Fattori, C. Fort, M. Zaccanti, G. Modugno, M. Modugno, and M. Inguscio. *Anderson localization of a non-interacting Bose-Einstein condensate*. Nature **453**, 895–898 (2008).
- [10] M. Fattori, G. Roati, B. Deissler, C. D’Errico, M. Zaccanti, M. Jona-Lasinio, L. Santos, M. Inguscio, and G. Modugno. *Magnetic dipolar interaction in a Bose-Einstein condensate atomic interferometer*. Phys. Rev. Lett. **101**, 190405 (2008).

- [11] R. J. Fletcher, A. L. Gaunt, N. Navon, R. P. Smith, and Z. Hadzibabic. *Stability of a Unitary Bose Gas*. Phys. Rev. Lett. **111**, 125303 (2013).
- [12] C. Cabrera, L. Tanzi, J. Sanz, B. Naylor, P. Thomas, P. Cheiney, and L. Tarruell. *Quantum liquid droplets in a mixture of Bose-Einstein condensates*. arXiv:1708.07806 (2017).
- [13] G. Roati, M. Zaccanti, C. D’Errico, J. Catani, M. Modugno, A. Simoni, M. Inguscio, and G. Modugno. *^{39}K Bose-Einstein condensate with tunable interactions*. Phys. Rev. Lett. **99**, 010403 (2007).
- [14] M. Landini, S. Roy, G. Roati, A. Simoni, M. Inguscio, G. Modugno, and M. Fattori. *Direct evaporative cooling of ^{39}K atoms to Bose-Einstein condensation*. Phys. Rev. A **86**, 33421 (2012).
- [15] G. Salomon, L. Fouché, S. Lepoutre, A. Aspect, and T. Bourdel. *All-optical cooling of ^{39}K to Bose-Einstein condensation*. Phys. Rev. A **90**, 33405 (2014).
- [16] H. J. Metcalf and P. Van der Straten. *Laser cooling and trapping* (Springer Science & Business Media, 2012).
- [17] C. J. Foot. *Atomic physics* (Oxford University Press, 2005).
- [18] C. J. Pethick and H. Smith. *Bose-Einstein condensation in dilute gases*. 2nd ed. (Cambridge University Press, 2002).
- [19] T. G. Tiecke. *Properties of Potassium*. (2011).
<http://www.tobiastiecke.nl/archive/PotassiumProperties.pdf>.
- [20] C. N. Cohen-Tannoudji and W. D. Phillips. *New Mechanisms for Laser Cooling*. Phys. Today **43**, 33–40 (1990).
- [21] J. Dalibard and C. Cohen-Tannoudji. *Laser cooling below the Doppler limit by polarization gradients: simple theoretical models*. J. Opt. Soc. Am. B **6**, 2023–2045 (1989).
- [22] G. Salomon, L. Fouché, P. Wang, A. Aspect, P. Bouyer, and T. Bourdel. *Gray-molasses cooling of ^{39}K to a high phase-space density*. EPL **104**, 63002 (2013).
- [23] C. D’Errico, M. Zaccanti, M. Fattori, G. Roati, M. Inguscio, G. Modugno, and A. Simoni. *Feshbach resonances in ultracold ^{39}K* . New J. Phys. **9**, 223 (2007).
- [24] H. F. Hess. *Evaporative cooling of magnetically trapped and compressed spin-polarized hydrogen*. Phys. Rev. B **34**, 3476–3479 (1986).
- [25] W. Müssel. *Characterization of a Two-dimensional MOT for ^{39}K* . Master’s thesis. University of Heidelberg (2011).

- [26] J. M. Gerton, D. Strekalov, I. Prodan, and R. G. Hulet. *Direct observation of growth and collapse of a Bose-Einstein condensate with attractive interactions.* Nature **408**, 692–695 (2000).
- [27] J. L. Roberts, N. R. Claussen, S. L. Cornish, E. A. Donley, E. A. Cornell, and C. E. Wieman. *Controlled collapse of a Bose-Einstein condensate.* Phys. Rev. Lett. **86**, 4211–4214 (2001).
- [28] K. Dieckmann, R. J. C. Spreeuw, M. Weidemüller, and J. T. M. Walraven. *Two-dimensional magneto-optical trap as a source of slow atoms.* Phys. Rev. A **58**, 3891–3895 (1998).
- [29] I. Stroescu. *On a cold beam of potassium atoms.* Master’s thesis. University of Heidelberg (2010).
- [30] I. Stroescu. *Dissipative Double-Well Potential: Mesoscopic Atom Number Detection and Cold Atom Dynamics.* Ph.D. thesis. Universität Heidelberg (2014).
- [31] I. Stroescu, D. B. Hume, and M. K. Oberthaler. *Double-well atom trap for fluorescence detection at the Heisenberg limit.* Phys. Rev. A **91**, 013412 (2015).
- [32] F. V. Nicolai. *Design and construction of a fiber-coupled tapered amplifier system.* Master’s thesis. University of Heidelberg (2017).
- [33] A. F. Impertro. *Construction of a laser setup in a Potassium-BEC-Experiment.* Bachelor’s thesis. University of Heidelberg (2017).
- [34] J. D. Jackson. *Klassische Elektrodynamik.* 4th ed. (Walter de Gruyter, 1999).
- [35] Huntsman. *Technical Datasheet Araldite F.* (2015).
<http://www.aralditematerials.com/us/tds/322-araldite-f-ci-aradur-hy-905-ci-dy-040-ci-dy-062-ci-dy-073-1-ci-silica-apac-e/file.html>.
- [36] M. Sparn. *Magnetic Fields for Cooling and Trapping of Potassium Atoms.* Bachelor’s thesis. University of Heidelberg (2017).
- [37] P. Horowitz and W. Hill. *The Art of Electronics.* 2nd ed. (Cambridge University Press, 1989).
- [38] M. Landini. *A tunable Bose-Einstein condensate for quantum interferometry.* Ph.D. thesis. Università degli Studi di Trento (2011).
- [39] J. Berges, A. Rothkopf, and J. Schmidt. *Nonthermal fixed points: Effective weak coupling for strongly correlated systems far from equilibrium.* Phys. Rev. Lett. **101**, 041603 (2008).

Worte des Dankes

Zunächst möchte ich mich bei Markus Oberthaler bedanken, der mir diese Masterarbeit und auch die weitere Arbeit am BECK ermöglicht hat. Dein Optimismus und Interesse an der Physik sind wirklich motivierend.

Darüber hinaus danke ich Fred Jendrzewski für die Zweitkorrektur dieser Arbeit.

Helmut, Dir danke ich für viele Erklärungen und Diskussionen. Dein Wissensdurst und Deine Neugierde sind bewundernswert und ansteckend. Ich habe mich am Experiment von Anfang an wohl gefühlt und die Zusammenarbeit – ob am Experiment, in der Werkstatt oder im Baumarkt – hat großen Spaß gemacht.

Celia, vielen Dank für deine Unterstützung und die gute Zusammenarbeit. Ich freue mich auf die kommenden Jahre und die Physik, an der wir manchmal verzweifelt, aber immer auch gewachsen sind.

Alex und Marius danke ich für die gute Zeit im Labor und interessante Diskussionen.

Zhongyi und Lisa, es war und ist mir eine Ehre mit Euch im gleichen Büro zu sitzen und über Gewindenormen und mehr zu diskutieren. Auch wenn es manchmal wegen Pfandflaschenbasketball etwas gefährlich wird.

Philipp und Max, vielen Dank für Eure Unterstützung besonders auch gegen Ende meines Masterjahres.

Dem ganzen Team danke ich für die gemeinsame Zeit. Ob beim Abendessen im Botanik, beim Frühstück am Freitagmorgen, beim Drachenbootcup oder diversen Grillabenden, das offene und angenehme Klima in der Gruppe sorgt für ein gutes Miteinander. Das gegenseitige Interesse ist sehr motivierend. Ich freue auf die nächsten Jahre.

Felix, vielen Dank für das gute Miteinander über die vielen Jahre, die schöne Zeit in Heidelberg und Deine Unterstützung.

Carmen, danke für Deine Unterstützung und die schöne gemeinsame Zeit. Ich freue mich, dass es Dich gibt.

Zuletzt möchte ich meiner ganzen Familie danken. Ihr habt mich immer unterstützt und es ist wirklich wunderbar, dass ich mich immer auf Euch verlassen kann!

Erklärung

Hiermit versichere ich, diese Arbeit selbstständig verfasst und keine anderen als die angegebenen Quellen verwendet zu haben.